Supporting Information

Safe Seasonal Energy and Hydrogen Storage in a 1:10 Single-Household-Sized Pilot Reactor Based on the Steam-Iron Process

*Samuel P. Heiniger, Zhiyuan Fan, Urs B. Lustenberger, and Wendelin J. Stark**
ETH Zürich, Vladimir-Prelog-Weg 1, 8093 Zürich, Switzerland
E-mail: wendelin.stark@chem.ethz.ch

Supplementary Note 1. Materials and Methods

Chemicals and supplies: H_2 (PanGas, 5.0) was supplied in 50 L bottles at 200 bar g. N_2, cooling water and deionized water were supplied by ETH Zürich through pipelines. Bayferrox® 306 (BF306) was manufactured by Lanxess using Laux process. The iron ore powder was obtained from an iron ore pit in Ukraine.

Density measurement: The untapped density was determined by filling a 250 mL measuring cylinder carefully without vibration and applied downward pressure and then measuring the weight change. Each sample was measured three times. The tap density was measured using a Pycnometer Micromeritics GeoPyc 1360 with a force of 114 N on a cyclinder with 38.1 mm diameter, corresponding to 1 bar pressure. Each sample was measured 7 times.

Thermogravimetric analysis (TGA): The TGA was performed on a Linseis STA PT1600 thermogravimetric analyzer with a L40/2054 external gas dosing system. 5-6 mg of iron oxide was used in each measurement. The sample was heated to the target temperature, after which repeated reduction/oxidation cycles were conducted in wet H_2 and wet N_2. Wet H_2 was obtained by passing H_2 through a water bubbler at room temperature, and subsequently cooling of the gas to around 10 °C using cooling water, exactly mimicking the process in the pilot reactor (condenser). Wet N_2 was obtained by passing dry N_2 through water at room temperature, without further cooling. For all 20-cycle experiments, one cycle comprised of 2 h reduction and 2 h oxidation. The temperature, relative humidity and flow rate of the off-gas were monitored using Sensirion SHT41 and SFM4100 sensors. All measurements were corrected by subtracting a blank experiment with no sample loaded in the crucible.

X-ray diffraction (XRD) analysis: The XRD pattern was measured on a PANalytical X'Pert Pro MPD device using Cu Kα1 radiation. The settings of the X-ray tube were 40 kV and 45 mA. The diffraction intensity was scanned from $2\theta = 10\text{-}90°$, at a step size of 0.017° and a scanning speed of 2.1 s per step. The samples taken from the reactor were imbedded in GE Bayer high viscosity silicon grease in roughly 1:4 mass ratio to prevent oxidation during measurement, while other samples were measured as they were.

Brunauer-Emmett-Teller (BET) surface area measurement: The specific surface area was measured by N_2 sorption at 77 K. Two instruments were used. The surface area of BF306, iron ore and the iron taken from the reactor after re-oxidation in air was measured on a Micromeritics TriStar II 3020 device. The samples were degassed at 250 °C and < 0.5 mbar overnight. Iron taken from the reactor was measured on a Belsorp mini II device, which was able to avoid the contact between the sample and air during sample transfer. The samples were stored and loaded into the sample holder in an Ar glovebox, and were not degassed prior to measurement.

Scanning electron microscopy (SEM): The morphology of iron oxide samples was observed in a FEI Nova NanoSEM 450 scanning electron microscope. The samples were prepared as 0.2 mg mL^{-1} suspension in isopropanol and ultrasonicated for 5 min to disperse the particles. 2 μL of suspension was pipetted to a copper grid, which was then dried under an IR lamp. The grid was then loaded in the SEM for image acquisition. The acceleration voltage was 15 kV; the spot size was 2.0; the working distance was 6.0-6.5 mm; and TLD detector was used in immersion mode.

Element analysis: The elemental contents of C, H, N, and S in the iron oxide samples were determined on an Elementar Vario Macro Cube elemental analyzer. The samples were further tested for their contents of Al, Ca, Cr, Fe, Co, Cu, Mg, Ni, and Zn using inductively coupled plasma analysis by Bachema AG.

Safety demonstration: In total, around 15 kg of iron powder was obtained from the reactor. Around 400 g of it was poured into a 16 cm wide and 7 cm high ceramic bowl in laboratory air. The powder was stirred with a stainless-steel spatula and left untouched. The appearance and temperature were recorded with an optical camera (Samsung S20 FE) and an IR camera (Flir E40), both at 50 cm distance. The IR camera had a measurement range of 0-670 °C, and the emissivity of the sample was assumed to be 0.95 (the highest setting of the camera). The lighting in the laboratory was turned off, to better observe how the iron was visually glowing. For attempted grilling of sausages (common Swiss sausages, “Cervelat”, a standardized product), around 1 kg of iron powder was poured into a 25 cm wide ceramic bowl in open air (at an outdoor grilling spot), and two sausages were placed at around 30 cm above the iron powder for 15 min. Both the optical and IR images were recorded. **Please note that the active iron powder involved in this study is very reactive, and reacts rapidly with oxygen when exposed in air. This could result in high temperature or even dust explosion.**

Table S1. Abbreviations and Definitions

Definition	Abbreviation
Power supplied	P
Time	t
Efficiency	η
Difference of power between production and demand	Δ
Installed PV capacity per total demand	x
Annualized Cost	C
Cost factor	c
Size	S
Interest rate	r
Level of self sufficiency	SS
Levelized Cost of Energy	$LCOE$
Winter	w
Day	d
Fuel cell	FC
Seasonal storage	S
Battery	B
Electrolyzer	El
Demand	D
Photovoltaic	PV
Liquid organic hydrogen carriers	LOHC
Liquid natural gas	LNG

Supplementary Note 2. Calculation of the mismatch between the PV production and electricity demand

The PV production is computed by averaging the different generation curves as referenced in.[1] The generation curves of the different PV types and productivity classes are multiplied with they're corresponding capacity potential and the sum of the resulting curves is normalized with the total capacity potential. The electricity demand data used in this publication is obtained from the swiss national electricity grid operator SwissGrid,[2]
The data for the year 2017 is used in this analysis. The electricity demands in New Zealand, China, Brazil and the US represent estimations for the year 2020.[3]

Supplementary Note 3. Calculation of the relationship between self-sufficiency with the installed PV capacity

The scenario without storage is calculated by summing the differences between demand $D(t)$ and production $x\,PV(t)$, the electricity deficits $\Delta(t)$ for the first 60 days and the last 30 days of the year (1), which correspond to the winter months. The sum over the deficits is then summed and normalized with the total electricity demand during the winter months (2). The resulting fraction describes the energy lacking during the winter months, which corresponds to the complement of the level of self-sufficiency, which is computed for ratios of annual PV production to annual demand x.

$$\Delta(t) = \begin{bmatrix} D(t) - x\,PV(t) & if\ \Delta(t) > 0 \\ 0 & else \end{bmatrix} \#(1)$$

$$SS = 1 - \frac{\sum_{t_w} \Delta(t)}{\sum_{t_w} D(t)} \#(2)$$

The scenario with additional day-night storage sums up the differences $\Delta_d(t)$ between surpluses and deficits for each day (3). The surpluses are multiplied with the round-trip efficiency of Li-ion batteries η_B accounting for losses during the storage process.^{4} Overall surpluses may not exceed the overall deficits, the additional surpluses are lost due to lack of longer duration energy storage. The self-sufficiency in winter corresponds to complement of the sum of the deficits during the winter months divided by the total demand during winter (5).

$$\Delta_d(t) = \begin{bmatrix} \sum_{t_d} [D(t) - x\,PV(t)]\varphi_1(t) & if\ \Delta_d(t) > 0 \\ 0 & else \end{bmatrix} \#(3)$$

$$\varphi_1(t) = \begin{bmatrix} 1 & if\ \Delta(t) > 0 \\ \eta_B & else \end{bmatrix} \#(4)$$

$$SS = 1 - \frac{\sum_{t_w} \Delta_d(t)}{\sum_{t_w} D(t)} \#(5)$$

The differences between production and consumption are summed up as in the scenario with day-night storage. However, seasonal storage allows for the inter day redistribution of energy. To account for the stored energy, $\Delta_d(t)$, the deficit within a day is multiplied with ρ (6), a parameter describing the ratio of the remaining deficit after inter-day exchange with the total amount of energy requested by the deficit days before the integration (7).

The deficit after inter-day exchange is computed by subtracting the energy difference at the surplus days times the seasonal storage efficiency (20 %, the lower limit from^5) from the deficit days. The self-sufficiency then corresponds to the complement of the sum over all adjusted deficit days during the winter month divided total demand in winter (9).

$$\Delta_s(t) = \begin{bmatrix} \sum_{t_d} \rho[D(t) - x\,PV(t)] & if\ \Delta_d(t) > 0 \\ 0 & else \end{bmatrix} \#(6)$$

$$\rho = \begin{bmatrix} \dfrac{\sum_{t_a} \Delta_d \varphi_2(t)}{\sum_{t_a, \Delta_d > 0} \Delta_d} & if \sum_{t_d} \Delta_d \varphi_2(t) > 0 \\ 0 & else \end{bmatrix} \#(7)$$

$$\varphi_2(t) = \begin{bmatrix} 1 & if\ \Delta_d(t) > 0 \\ \eta_S & else \end{bmatrix} \#(8)$$

$$SS = 1 - \frac{\sum_{t_w} \Delta_s(t)}{\sum_{t_w} D(t)} \#(9)$$

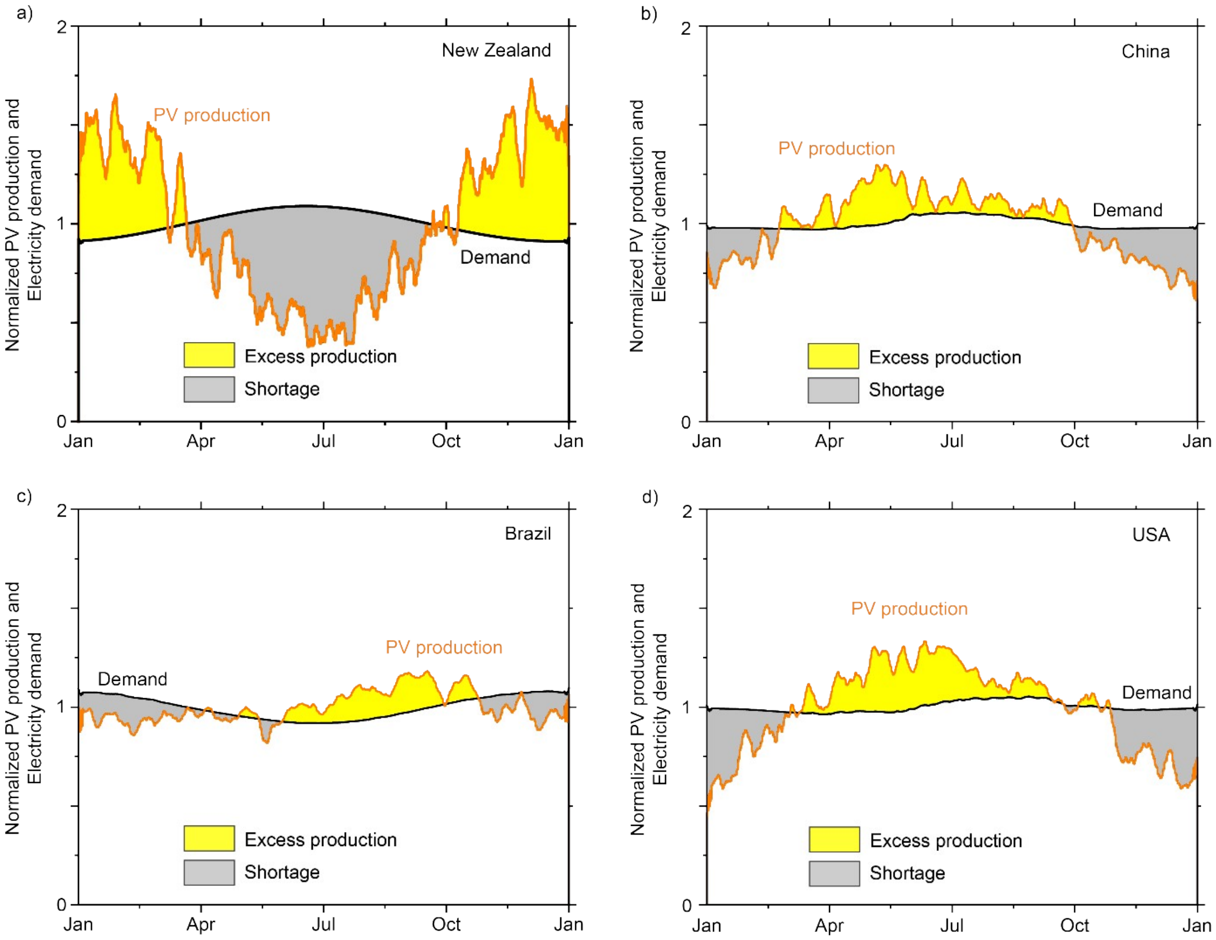

Figure S1. Normalized PV production and electricity demand over a one-year period. The mismatch between production and demand necessitates energy storage on the time scale of six months for the countries a) New Zealand, b) China, c) Brazil and d) the United States

Table S2. The density, corresponding H_2 storage density and specific surface area of iron oxides tested in this work

FeO_x	Crystalline density[a)] g cm^{-3}	Particle density[b)] g cm^{-3}	Untapped density g cm^{-3}	Tapped density g cm^{-3}	Storage capacity[c)] kg H_2 m^{-3}	SSA_{BET} m^2 g^{-1}
BF306	5.18	4.6	1.02	1.51	28.4 - 42.1	9.98
Iron ore	5.18	-	2.12	2.80	59.1 - 78.0	0.88

[a)] The density of a perfect single crystal. [b)] The density of the particle as measured by the manufacturer according to ISO 787-10:1995. [c)] The mass of H_2 stored in Fe per unit volume, assuming 80% of the Fe is oxidized in the discharging step, with the upper and lower limit calculated from the untapped density and tapped density, respectively.

Supplementary Note 4. Experimental details about the reactor

Construction and operation: Accurate geometries and all construction details of the reactor and the 1st charging operation are described in detail in section 5.2 of the doctoral thesis of U. Lustenberger at ETH Zürich.[6] Briefly, the system consisted of a 0.21 m^3 packed bed reactor, a counter-current heat exchanger, a condenser with drain, an adsorption column, a compressor, an evaporator, and some solenoid valves for fluid control. The reactor was made of 316L stainless steel. The internal diameter was 590 mm, and the internal height was 762 mm. The reactor was filled with around 250 kg of BF306. The reactor was externally electrically heated on the jacket and on the bottom. The jacket heater and bottom heater had a maximum power of 1304 W and 520 W, respectively. Both heaters could be individually controlled using PID controller. The temperature of the reactor was monitored with eight type-K thermocouples, T_1, T_2 on the top, T_3-T_6 on the jacket and T_7, T_8 on the bottom. Two safety valves were installed, one on the top cover of the reactor, one on the inlet of the reactor. The valves would depressurize the reactor should the pressure rises above 1.5 bar a. The inlet tube of the reactor was bent into a spiral with holes perforated at a certain interval, and located at the bottom of the reactor. The outlet of the reactor located on the top of the reactor. Gas travelled from the bottom to the top of the reactor through the entire reactor volume at all times. Two pressure sensors were installed at the inlet and outlet of the reactor, to measure the pressure drop. The off-gas was used to heat up the incoming gas in the heat exchanger. Both the reactor and heat exchanger were insulated with about 30 cm of rock wool. The off-gas was further cooled to around 10 °C in the condenser, with cooling water supplied by ETH Zürich through pipelines. The condensate could be removed through the drain. In charging mode, the off-gas was further dried by passing through the adsorption column filled with around 8.3 kg of dry silica gel. The gas was then recirculated back to the reactor through the compressor. The recirculation gas flow was monitored using a mass flow meter.

Data-logging: The data collected from the pilot plant was logged at a user-defined interval (usually every 1 min or 10 min) by the control software. The data for each calendar day were saved in a separate file. The following data was recorded at each time step:
No.: the serial number of the data point in the file;
Date: the date of the data point;
Time: the time of the data point;

T_1; T_2; T_3; T_4; T_5; T_6; T_7; T_8: the instantaneous temperatures (in °C) of the eight thermocouples;
MV_N2; MV_H2; MV_Re; MV_Pu; MV_Va; MV_Di; MV_Ga; MV_Wa: the instantaneous state of the solenoid valves, 1 = open, 0 = closed;
Pumpe Gas: the instantaneous state of the gas compressor, 1 = ON, 0 = OFF;
Pumpe Liquid: the instantaneous state of the water pump, 1 = ON, 0 = OFF;
P_1; P_2: the pressures measured by the two pressure sensors (in bar a);
MFM_IN; MFM_OUT: the instantaneous flow rates measured by the two mass flow meters (in g h^{-1});
Heater Mantel; Heater Boden: the instantaneous power output of the two heaters (in %);
IN_H2_full: describes the average flow rate of hydrogen supplied from a bottle to the reactor within the time interval between the current and the last measurement point. Two flow rates were recorded to avoid problems with solenoid valves closing and opening during the time interval.
IN_H2_part: describes the average flow rate of hydrogen supplied from a bottle to the reactor within the time interval between the current and the last measurement point, when valve MV_H2 was open; As a result, IN_H2_full is always smaller or equal to IN_H2_part;
IN_N2_full; IN_N2_part: the flow rates of N_2 flowing from the nitrogen supply to the reactor;
IN_Re_full; IN_Re_part: The recycle flow rate of gas recorded as long as the compressor is running (even when vacuuming the reactor and not recycling any gas). The flow rates are measured assuming pure hydrogen gas.
OUT_Di_full; OUT_Di_part: Flow rate of the gas leaving the reactor through the discharge valve. The flow rates are measured assuming pure hydrogen gas.

In addition to the automatically recorded data, the following parameters were recorded manually at least once per day during the operation of the reactor: the instantaneous jacket and bottom temperature; the instantaneous heating powers of the jacket and bottom heaters; the instantaneous pressures at the inlet and outlet of the reactor; the instantaneous flow rates at the two mass flow meters; the instantaneous weights of the water feed container and water collection container. The weights of old and new silica gel when exchanging the silica gel and the residual pressure in the old H_2 bottle after replacement were also recorded.

1st discharging of the reactor: In the beginning, liquid water was directly pumped into the heat exchanger and then into the reactor. At 213 h on stream, an evaporator was installed at the inlet of the heat exchanger, heating up the liquid water to steam at 200 °C. The pressure upper set point (measured by P_1) of the reactor, ranging between 1.0 and 1.2 bar a, was manually set, and was gradually increased during discharging. The pump ran until the pressure exceeded the upper set point, after which the pump was stopped. The outlet stayed open, until the pressure dropped to below the lower set point, which was 0.005-0.01 bar lower than the upper set point, when the pump was restarted. The jacket and bottom temperature were controlled using thermocouples T_1 and T_7, and were set to 260 °C and 300 °C, respectively. The off-gas passed through the condenser and adsorption column (the silica gel was never replaced during discharging) before it was discharged, whose flow rate was measured by a mass flow meter.

Data of the 1st discharging operation: All automatically recorded data files were merged into a single file and imported into excel. The cumulative time was calculated as the difference between the time and the time at the first data point. The step time was calculated as the time interval between the current data point and the previous data point. The amount of H_2 was calculated by integrating OUT_Di_full over time. At each time step IF(OR(Pumpe Liquide>0; AND(MV_Di=1; P1>0.99)); 1; 0) was used to determine whether the reactor was currently discharging (1 = discharging; 0 = not discharging). “Time on stream” was computed as the cumulative time when the discharging program was running.

The manually recorded data were treated as follows. The cumulative time of the current data point was calculated. The time on stream was calculated by the linear interpolation of cumulative time, using the relation between the cumulative time obtained above between the time on stream and cumulative time. The amount of H_2 produced was estimated by computing the difference of the cumulative weight of water collected after and fed the reactor, assuming no side reactions. The humidity in the H_2 discharged was neglected. The overall conversion of the water into H_2 was calculated as the total reacted water (total fed water minus total collected water) divided by the total fed water. The instantaneous conversion of water to H_2 was calculated using the total weight of water fed and collected of two adjacent data points. Negative values of the conversion were manually removed.

The full data for the discharging, irrespective of whether the reactor was actually discharging or not, including the temperature of the eight thermocouples, the pressure at the inlet and outlet of the reactor, the heating power of the jacket and bottom heater, the H_2 production rate, and the cumulative amount of H_2 produced, are available in Fig. S2.

2nd charging of the reactor: After the reactor was discharged, it was charged in the following procedure. The upper and lower set points (measured by P_1) were maintained constant at 1.1 and 1.0 bar a, respectively. The H_2 inlet opened; H_2 was fed to the reactor until the upper set point was reached. The H_2 inlet was closed, and the compressor started recirculating the gas. In order for the reactor to be charged as quickly as possible, the compressor ran at full power, and the recycle flow rate was kept close to the upper measuring limit (150 $g\ h^{-1}$). The pressure decreased as H_2 was converted into water, then removed through condensation or adsorption. The compressor stopped when the lower set point was reached, and the H_2 inlet (connecting to the H_2 supply as pressure bottles) was opened again. The charging proceeded in a periodical behavior. The silica gel in the drying column was replaced at a certain interval, usually once a week at the beginning of charging, and around twice as frequent at the end of charging. The jacket and bottom temperature were controlled by T_4 and T_7, and were set both to 425 °C. The bottom heater stopped working and had to be turned off at 683 h on stream.

Data of the 2nd charging operation: The data for charging operation were processed in a similar way. The automatically collected data was merged and imported into excel, the cumulative time and time step were calculated. The amount of H_2 fed to the reactor was calculated by integrating the IN_H2_full over time. The pressure drop of the reactor was calculated as the difference between P_1 and P_2. At each time step IF(OR(IN_Re_full at the current point>1; AND(IN_Re_full at the previous point>1; IN_H2_full at the current point >0));1;0) was used to determine whether the reactor was currently charging (1 = charging; 0 = not charging). "Time on stream" was computed as the cumulative time when the discharging program was running.

For the manually recorded data, the cumulative time was calculated, and the time on stream could be obtained by linear interpolation. The amount of H_2 consumed was estimated as the sum of the weight of the condensed and adsorbed water, assuming no side reactions. Additionally, the amount of H_2 consumed was estimated by computing the consumed H_2 after changing the bottle. The residual weight of H_2 in the bottle was calculated assuming the ideal gas law. The pressure was read from the pressure reducing valve, and a constant bottle volume of 50 L and a constant room temperature of 298 K were assumed. As specified by the supplier, each new bottled contained 747 g H_2.

The steam fraction in the reactor outlet was estimated as follows. The cumulative amount of recycled hydrogen was calculated by integrating IN_Re_full over the time.
The cumulative amount of recycled H_2 corresponding to the different data points in the manual file was calculated by linear interpolation. The steam fraction was then calculated by dividing the change in the amount of condensed water within a time with the amount recycled H_2 recycled (both in mole). Additionally, 1.23% was added to correct for the steam remaining in the recycled H_2, which was estimated based on the outlet temperature of the condenser (10 °C). This may introduce error at the end of charging cycle, when the steam fraction was low and very little or even no water condensed; or when the temperature of cooling water fluctuated. However, this is the best estimate when the humidity sensors at the condenser outlet were inoperative, and should be accurate enough for the majority of the charging operation, when a measurable amount of water was condensed.

The total amount of H_2 fed to the reactor, and the amount of H_2 fed to the reactor when it was being charged, could be calculated by integrating IN_H2_full over the cumulative time or over time on stream. The total amount of fed hydrogen are 5487 g and 5348 g, with a difference of only 139 g.

Three methods were used to calculate the SOC during charging. The first method, based on the total amount of hydrogen feed, shows a lower SOC than the other two methods (collected water and pressure difference in hydrogen bottles). A few explanations exist for this difference. H_2 was used for some purposes other than charging, mainly flushing the reactor to drive out the inert component, which could accumulate during charging, overestimating the SOC in the third way. However, the H_2 consumed for this purpose has been confirmed to be only 139 g. A small leakage might exist in the system, which would make the first and third way overestimate the SOC. However, the first way strongly underestimates compared with the second method, which produces similar results as the third, making this explanation unlikely. Another possibility is that the MFM was unable to accurately measure the flow of H_2, particularly when H_2 was fed within a short time interval. A similar phenomenon was also observed in the thesis (section 5.4.6.6)[6]. Thus, the results obtained in the second and third way are considered accurate.

The full data for the charging, irrespective of whether the reactor was actually charging or not, including the temperature of the eight thermocouples, the pressure at the inlet and outlet of the reactor, the heating power of the jacket and bottom heater, the recycle flow rate, and the cumulative amount of H_2 consumed, are available in Fig. S3.

Sampling the reactor after the 2nd charging operation: After the 2nd charging operation, both the jacket heater and the bottom heater were turned off, and the reactor was slowly cooled down to room temperature in H_2 atmosphere. H_2 was occasionally fed to the reactor to keep the pressure above the lower designed limit. After the reactor cooled completely, the atmosphere was replaced with N_2. The top cover of the reactor was then removed while being continuously flushed with N_2, and a custom-made sampling rod was used to take the sample from different depth, and later used for BET and XRD measurements. Around 15 kg of sample were also taken from the top of the reactor for safety demonstration. All samples were immediately transferred to a N_2 glove box (for samples used in BET measurement, an Ar glovebox was used) with <0.3 ppm H_2O and <1 ppm O_2 and stored there before use.

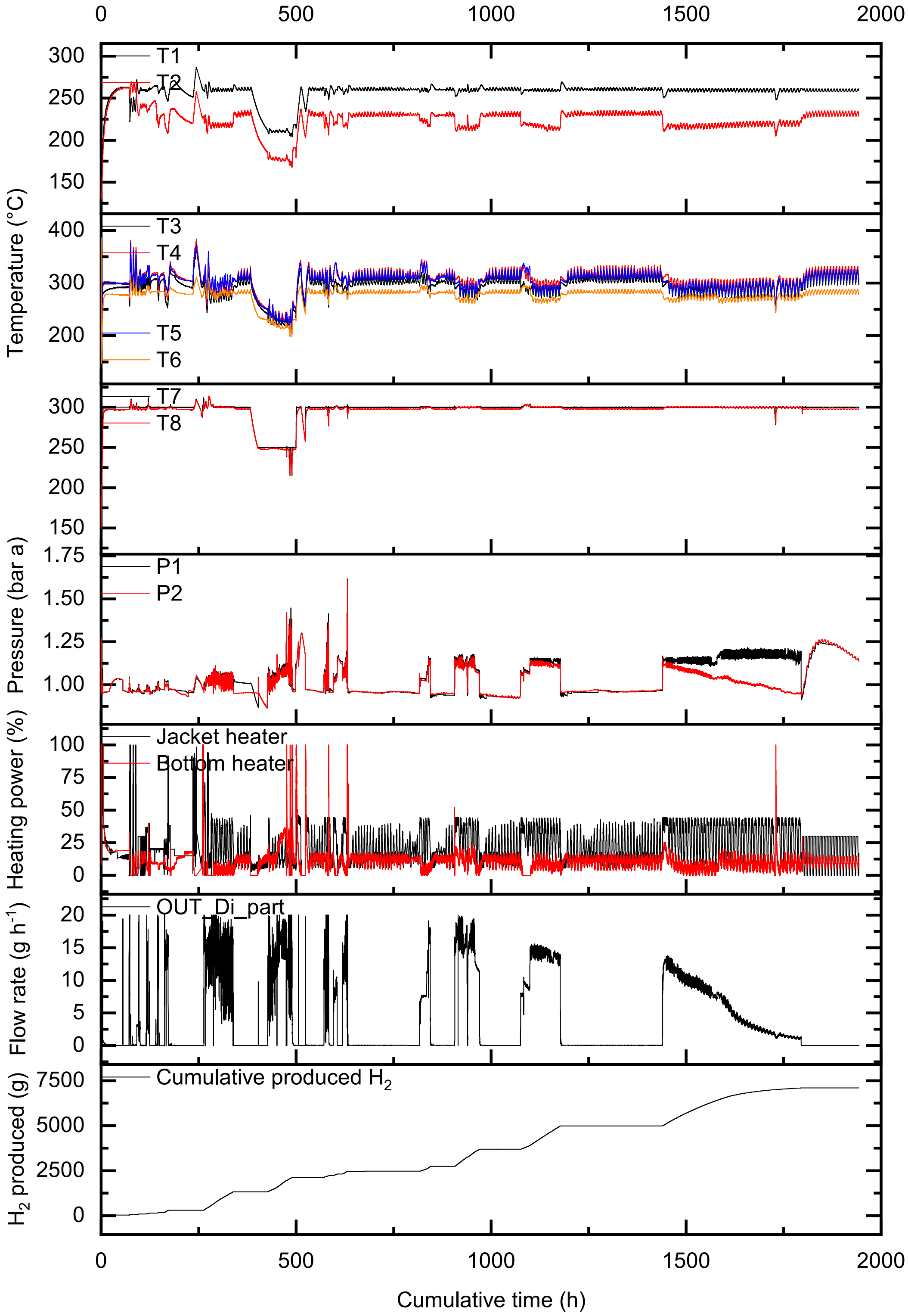

Figure S2. The temperature, pressure, heating power, H_2 production rate, and cumulative amount of H_2 produced during the 1st discharging.

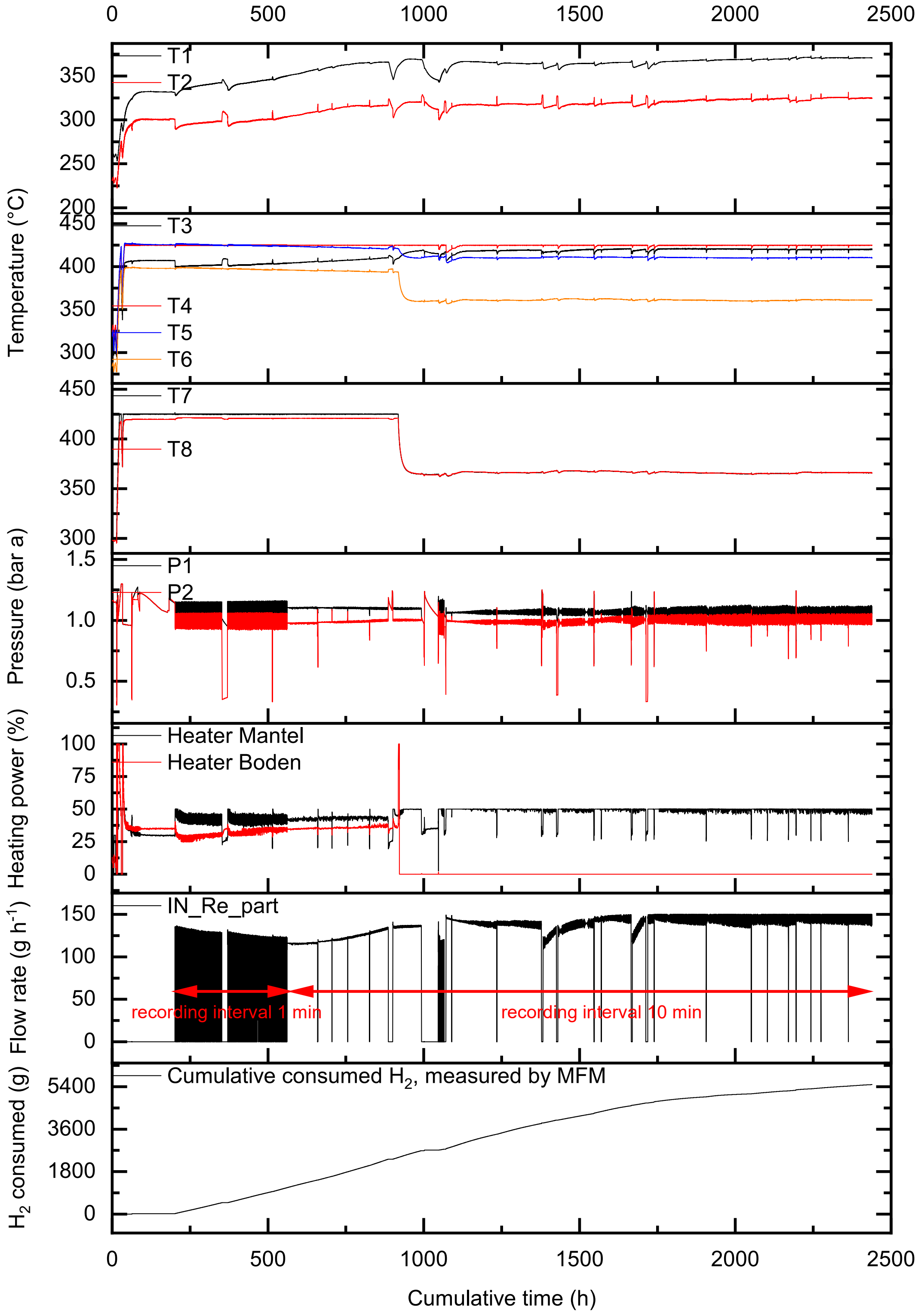

Figure S3. The temperature, pressure, heating power, recycle flow rate, and cumulative amount of H_2 consumed during the entire 2nd charging.

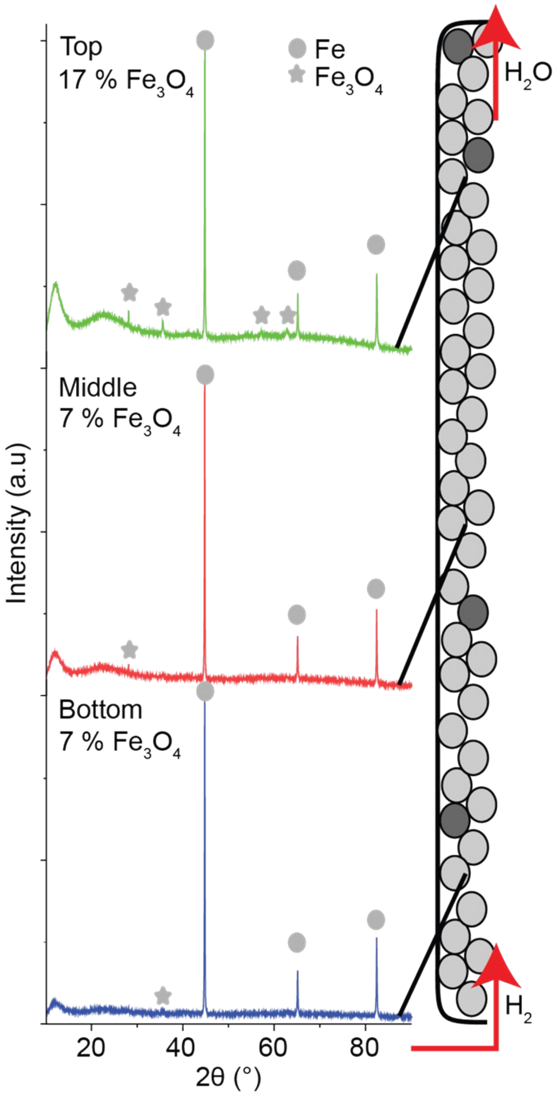

Figure S4. Quantitative X-ray diffraction measurements of samples taken from different reactor heights after the 2nd charging.

Table S3. Comparison between the 1st and 2nd charging

	1st charging	2nd charging
Jacket temperature setting (°C)	400 - 425	425
Final SOC (%)	88	84
Time to 80% SOC (h)[a)]	3179	1810
Proportion of water condensed (%)	33	63
Hydrocarbon formation	Yes	No

[a)] For the 1st charging, data point calculated from the raw data fitted to a first order decay model between 8% to 80% SOC. For the 2nd charging, direct readout from the raw data from 6.2% to 80% SOC.

Table S4. Elemental analysis of iron oxides

Elemental content	BF306	Iron ore
Fe wt%	61	64
C wt%	1.57	0.12
H wt%	0.39	0.00
N wt%	0.13	0.12
S wt%	0.00	0.46
Al mg kg^{-1}	1900	660
Ca mg kg^{-1}	<1000	<1000
Cr mg kg^{-1}	580	12
Co mg kg^{-1}	26	2
Cu mg kg^{-1}	1300	4
Mg mg kg^{-1}	<200	630
Ni mg kg^{-1}	170	9
Zn mg kg^{-1}	160	<2

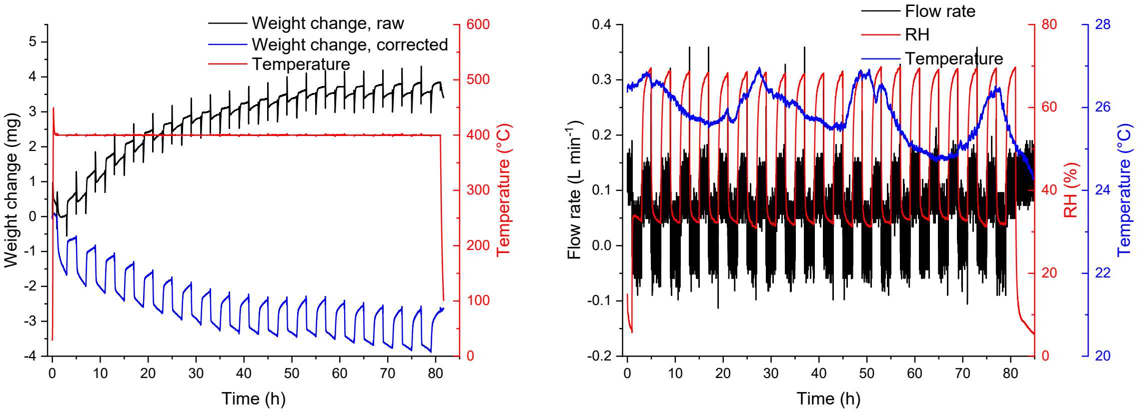

Figure S5. TGA data measured for a 5.84 mg BF306 sample at 400 °C over a period of 20 reduction oxidation cycles (a) Weight change and sample temperature: the raw weight change, the corrected weight change and the actual sample temperature over 20 cycles. (b) Off-gas parameters: the flow rate, relative humidity and temperature of the off-gas over 20 cycles. The flow rate of H_2 was unfortunately not measurable by the Sensirion SFM 4100 sensor.

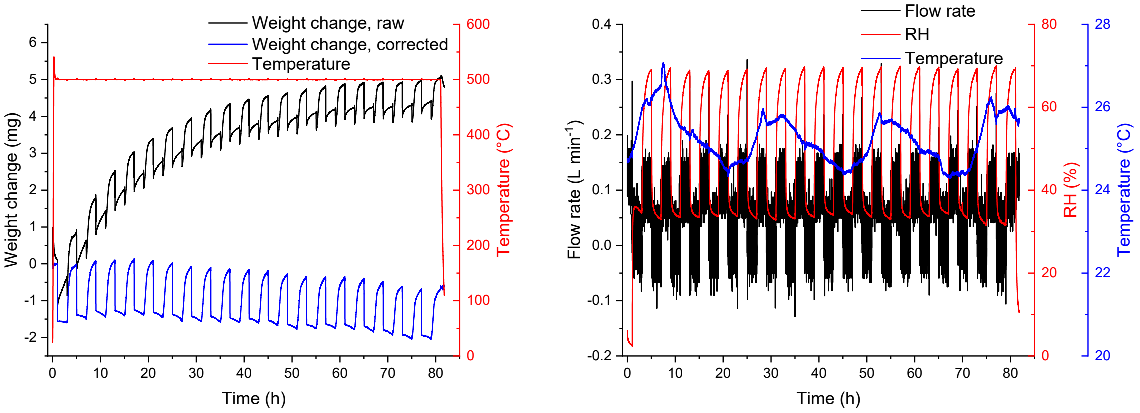

Figure S6. TGA data measured for a 5.67 mg BF306 sample at 500 °C over a period of 20 reduction oxidation cycles (a) Weight change and sample temperature: the raw weight change, the corrected weight change and the actual sample temperature over 20 cycles. (b) Off-gas parameters: the flow rate, relative humidity and temperature of the off-gas over 20 cycles. The flow rate of H_2 was unfortunately not measurable by the Sensirion SFM 4100 sensor.

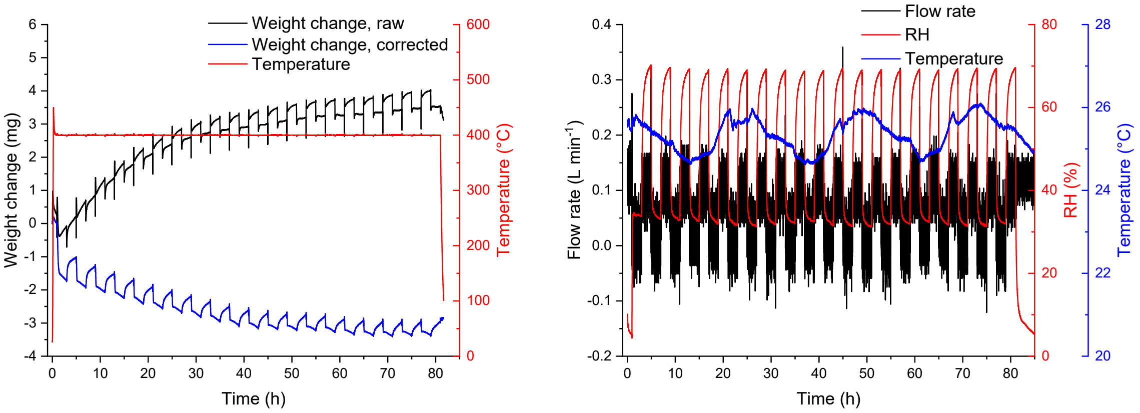

Figure S7. TGA data measured for a 5.27 mg iron ore sample at 400 °C over a period of 20 reduction oxidation cycles (a) Weight change and sample temperature: the raw weight change, the corrected weight change and the actual sample temperature over 20 cycles. (b) Off-gas parameters: the flow rate, relative humidity and temperature of the off-gas over 20 cycles. The flow rate of H_2 was unfortunately not measurable by the Sensirion SFM 4100 sensor.

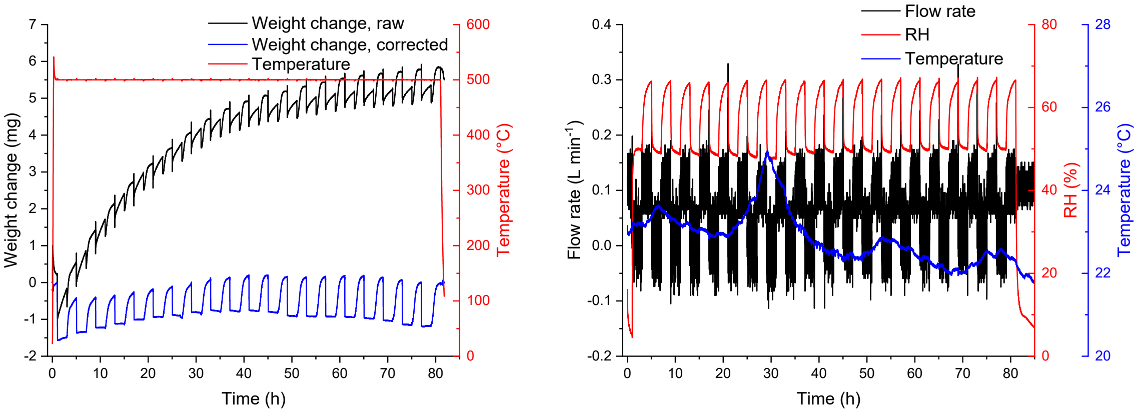

Figure S8. TGA data measured for a 5.87 mg iron ore sample at 500 °C over a period of 20 reduction oxidation cycles (a) Weight change and sample temperature: the raw weight change, the corrected weight change and the actual sample temperature over 20 cycles. (b) Off-gas parameters: the flow rate, relative humidity and temperature of the off-gas over 20 cycles. The flow rate of H_2 was unfortunately not measurable by the Sensirion SFM 4100 sensor.

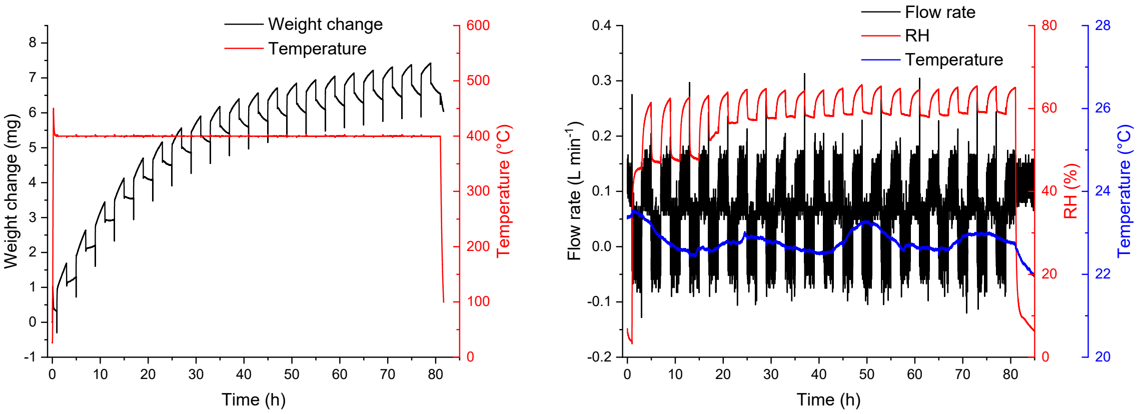

Figure S9. TGA correction data at 400 °C over a period of 20 reduction oxidation cycles (a) Weight change and sample temperature: the raw weight change and the actual sample temperature over 20 cycles. (b) Off-gas parameters: the flow rate, relative humidity and temperature of the off-gas over 20 cycles. The flow rate of H_2 was unfortunately not measurable by the Sensirion SFM 4100 sensor.

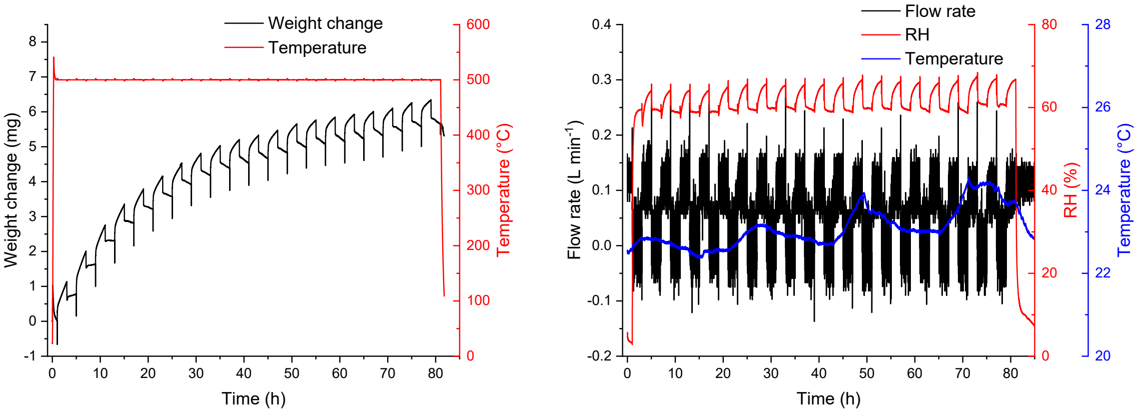

Figure S10. TGA correction data at 500 °C over a period of 20 reduction oxidation cycles (a) Weight change and sample temperature: the raw weight change and the actual sample temperature over 20 cycles. (b) Off-gas parameters: the flow rate, relative humidity and temperature of the off-gas over 20 cycles. The flow rate of H_2 was unfortunately not measurable by the Sensirion SFM 4100 sensor.

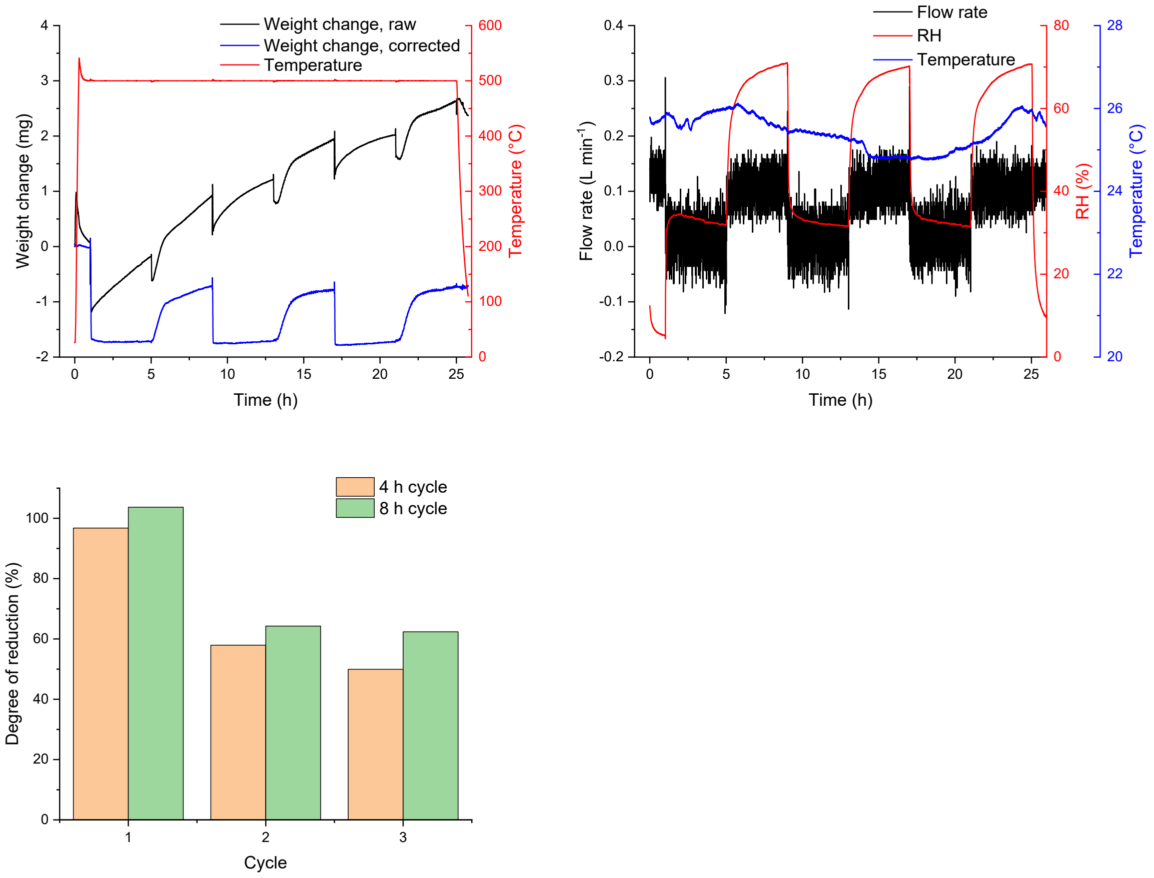

Figure S11. Influence of cycle time (4 h and 8 h) on the degree of reduction for iron ore at 500 °C. 5.76 mg iron ore was cycled 3 times for the 8 h cycle (a) Weight change and sample temperature: raw weight change, the corrected weight change and the actual sample temperature during three 8 h cycles. (b) Off-gas parameters: the flow rate, relative humidity and temperature of the off-gas over 20 cycles. The flow rate of H_2 was unfortunately not measurable by the Sensirion SFM 4100 sensor. (c) Comparison of the degree of reduction of the initial three cycles with 4 h and 8 h cycling times.

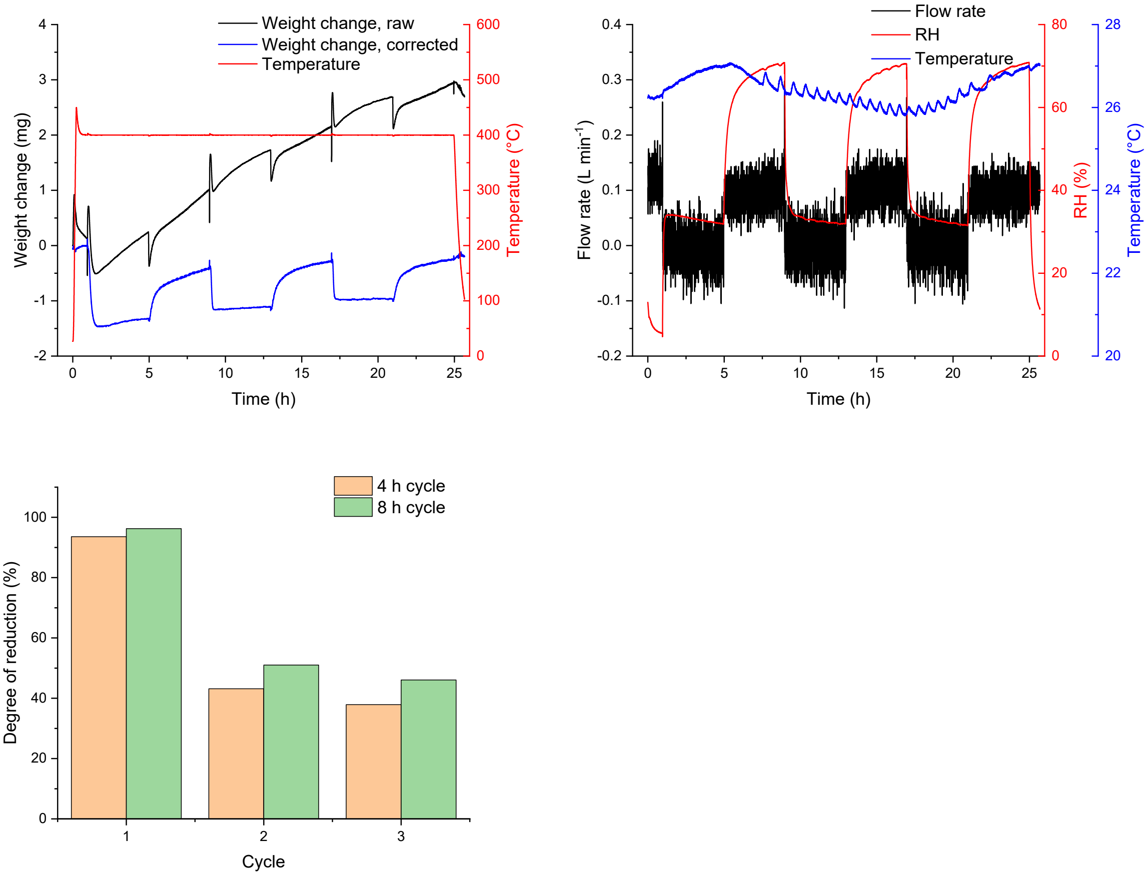

Figure S12. Influence of cycle time (4 h and 8 h) on the degree of reduction for iron ore at 400 °C. 5.49 mg iron ore was cycled 3 times for the 8 h cycle (a) Weight change and sample temperature: raw weight change, the corrected weight change and the actual sample temperature during three 8 h cycles. (b) Off-gas parameters: the flow rate, relative humidity and temperature of the off-gas over 20 cycles. The flow rate of H_2 was unfortunately not measurable by the Sensirion SFM 4100 sensor. (c) Comparison of the degree of reduction of the initial three cycles with 4 h and 8 h cycling times.

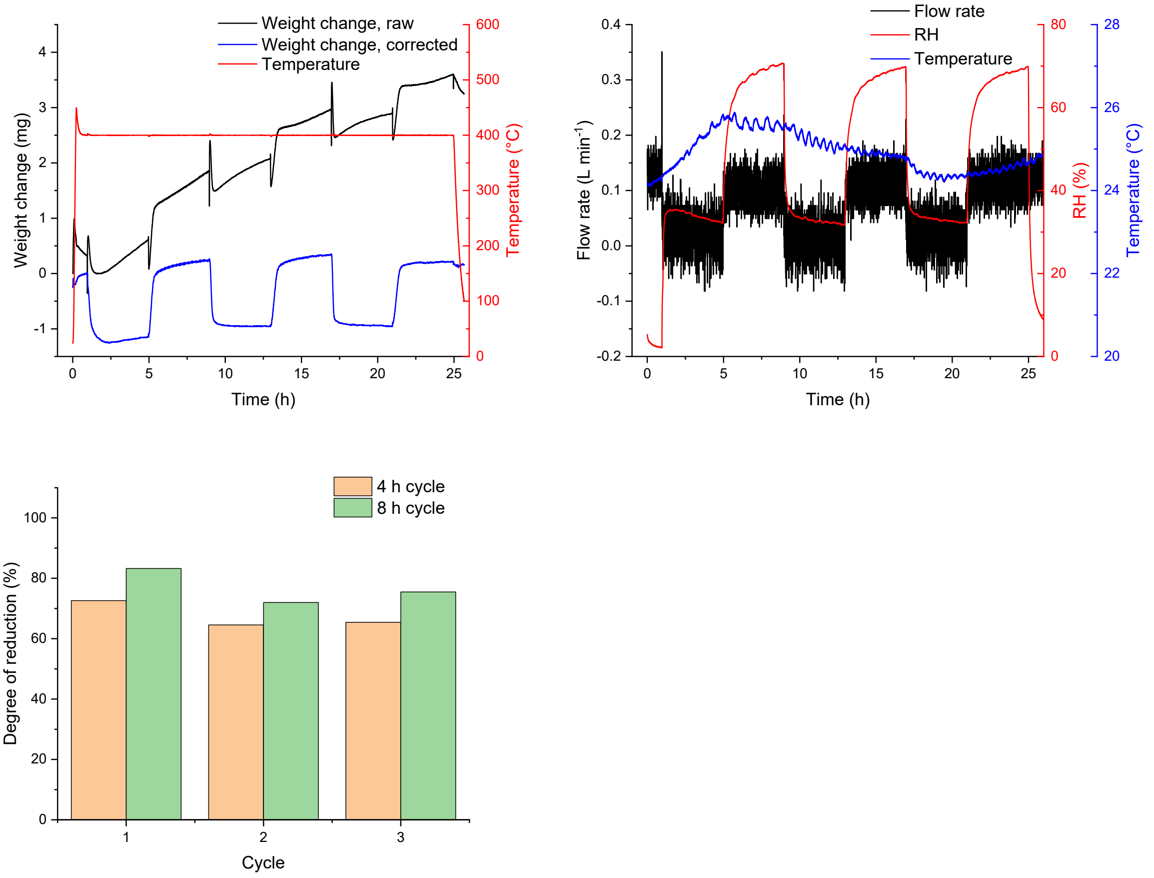

Figure S13. Influence of cycle time (4 h and 8 h) on the degree of reduction for BF306 at 400 °C. 5.65 mg BF306 was cycled 3 times for the 8 h cycle (a) Weight change and sample temperature: raw weight change, the corrected weight change and the actual sample temperature during three 8 h cycles. (b) Off-gas parameters: the flow rate, relative humidity and temperature of the off-gas over 20 cycles. The flow rate of H_2 was unfortunately not measurable by the Sensirion SFM 4100 sensor. (c) Comparison of the degree of reduction of the initial three cycles with 4 h and 8 h cycling times.

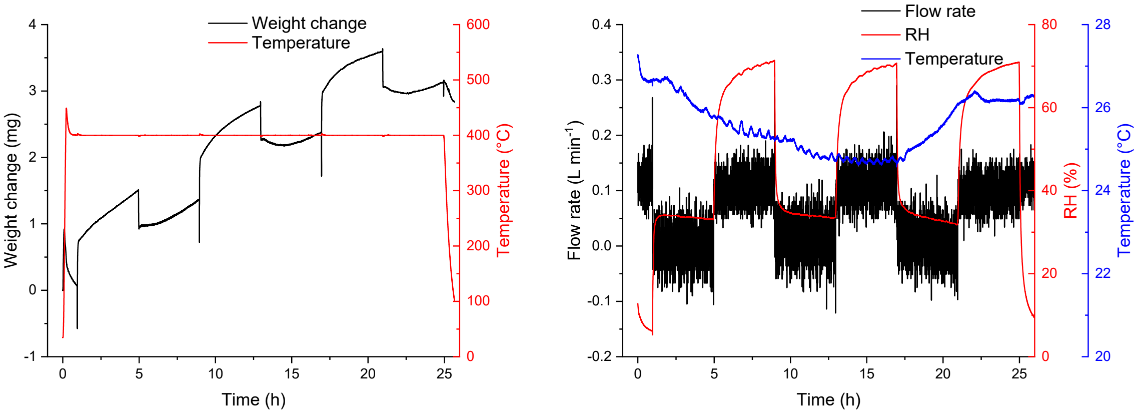

Figure S14. TGA correction data at 400 °C over a period of three 8 h reduction oxidation cycles (a) Weight change and sample temperature: the raw weight change and the actual sample temperature over 3 cycles. (b) Off-gas parameters: the flow rate, relative humidity and temperature of the off-gas over 3 cycles. The flow rate of H_2 was unfortunately not measurable by the Sensirion SFM 4100 sensor.

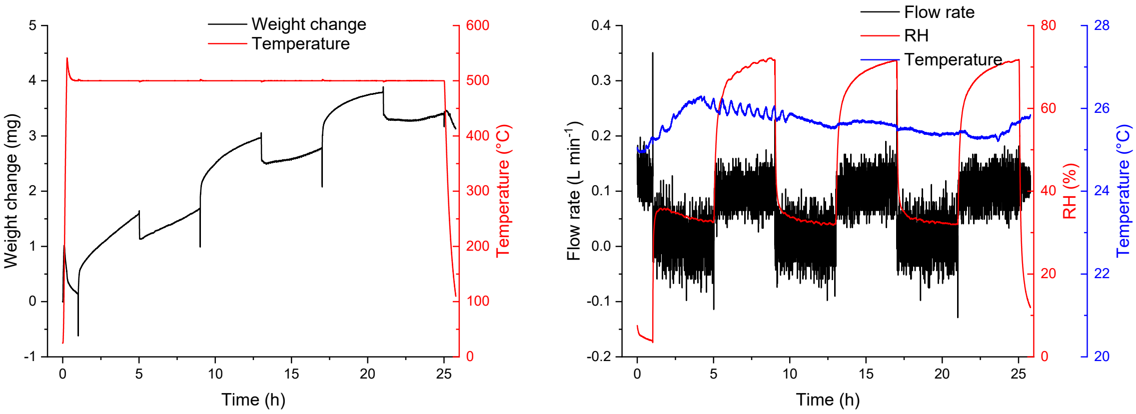

Figure S15. TGA correction data at 500 °C over a period of three 8 h reduction oxidation cycles (a) Weight change and sample temperature: the raw weight change and the actual sample temperature over 3 cycles. (b) Off-gas parameters: the flow rate, relative humidity and temperature of the off-gas over 3 cycles. The flow rate of H_2 was unfortunately not measurable by the Sensirion SFM 4100 sensor.

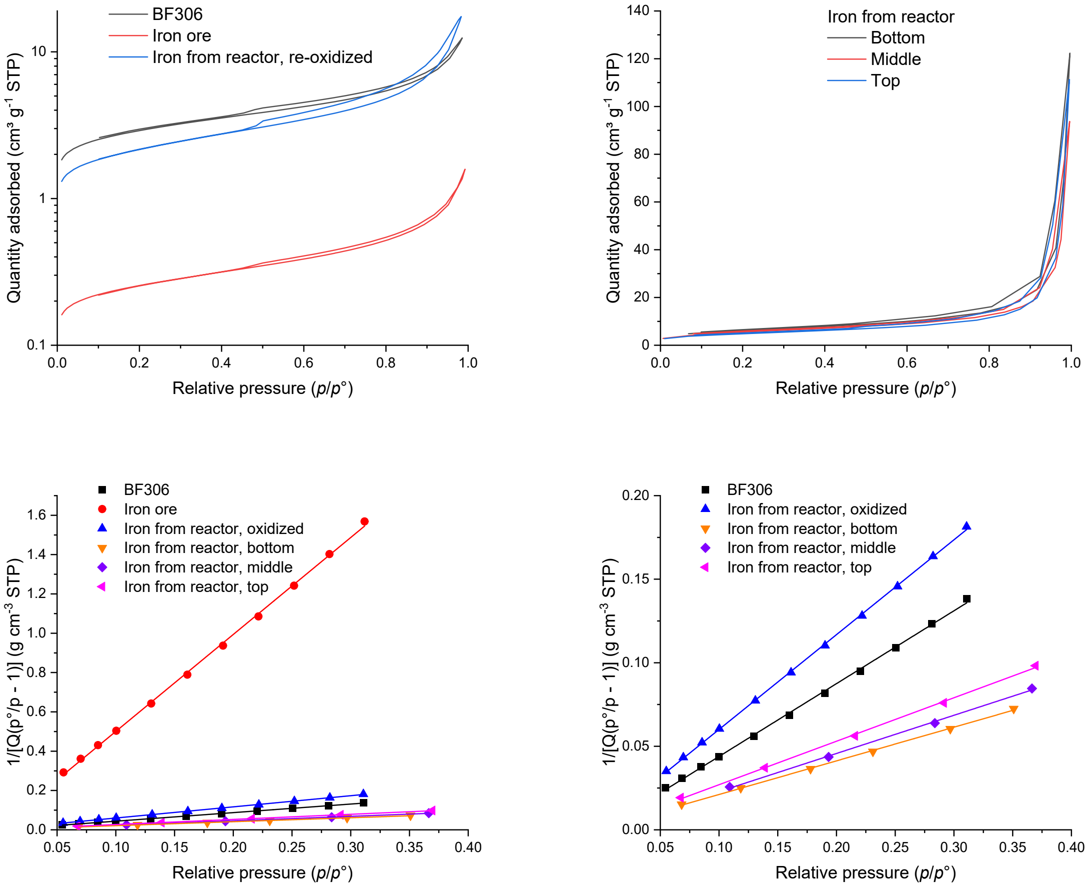

Figure S16. The N_2 adsorption and desorption isotherms at 77K, and the linear regression for BET surface area calculation

Table S5. The BET linear regression results and specific surface area

Sample	Slope g cm^{-3} STP	Intercept g cm^{-3} STP	R^2	SSA_{BET} m^2 g^{-1}
BF306	0.4359	0.0003	0.9991	9.98
Iron ore	4.9326	0.0073	0.9993	0.88
Iron from reactor, oxidized	0.5675	0.0033	0.9997	7.62
Iron from reactor, bottom	0.2013	0.0010	0.9991	21.52
Iron from reactor, middle	0.2285	0.0000	0.998	19.06
Iron from reactor, top	0.2602	0.0010	0.999	16.66

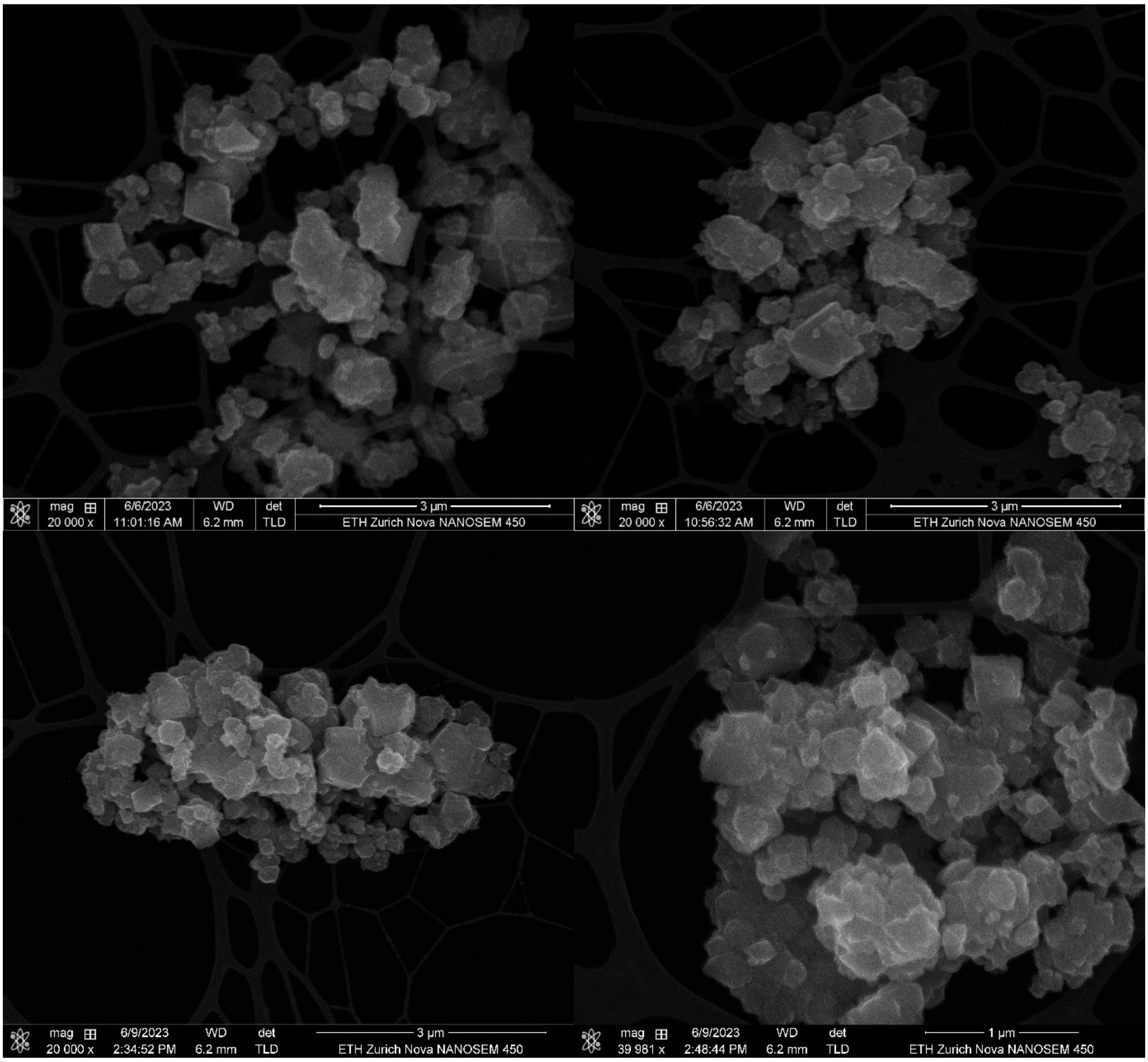

Figure S17. SEM images of BF306.

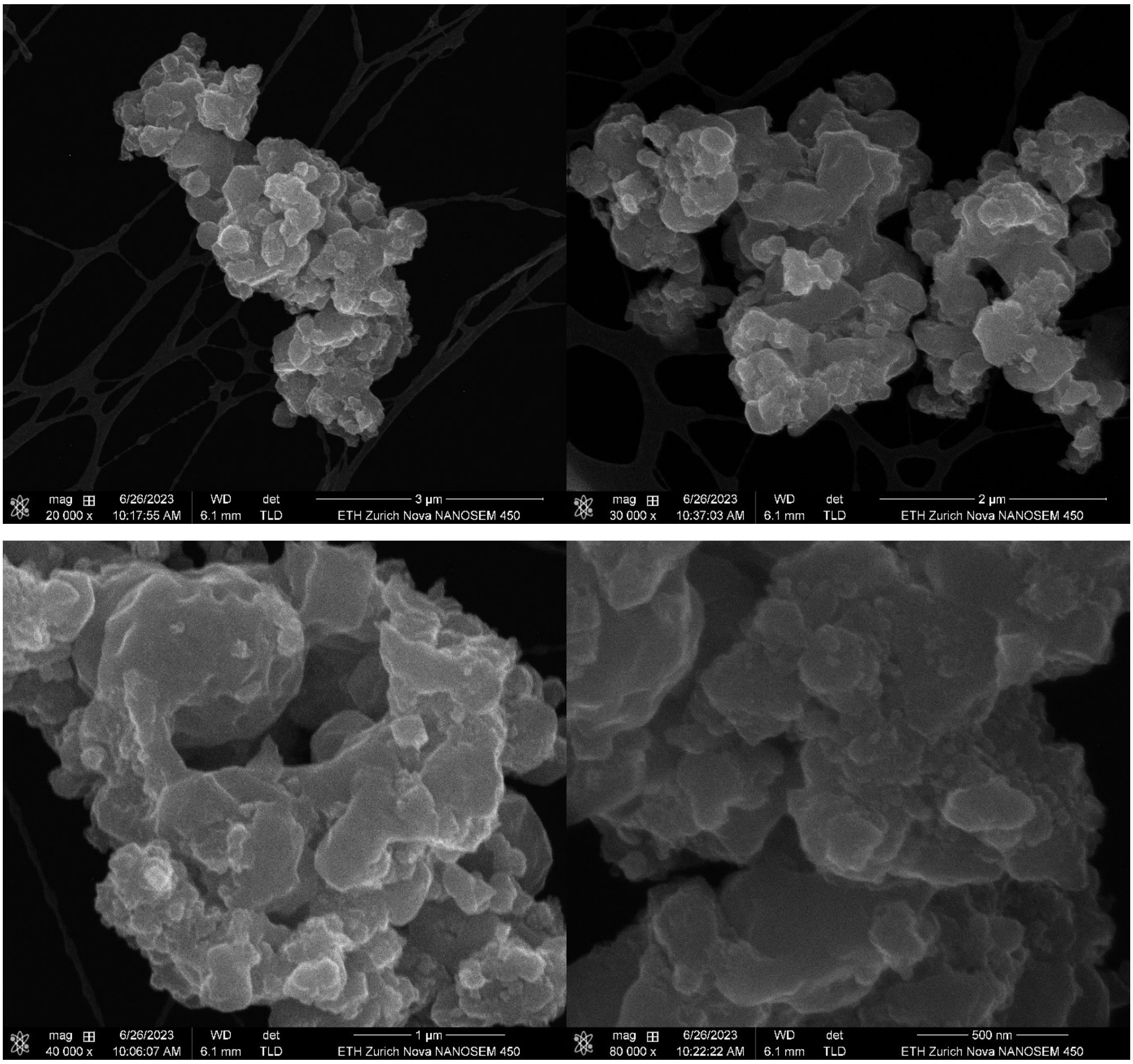

Figure S18. SEM images of BF306 after 20 cycles on TGA at 400 °C

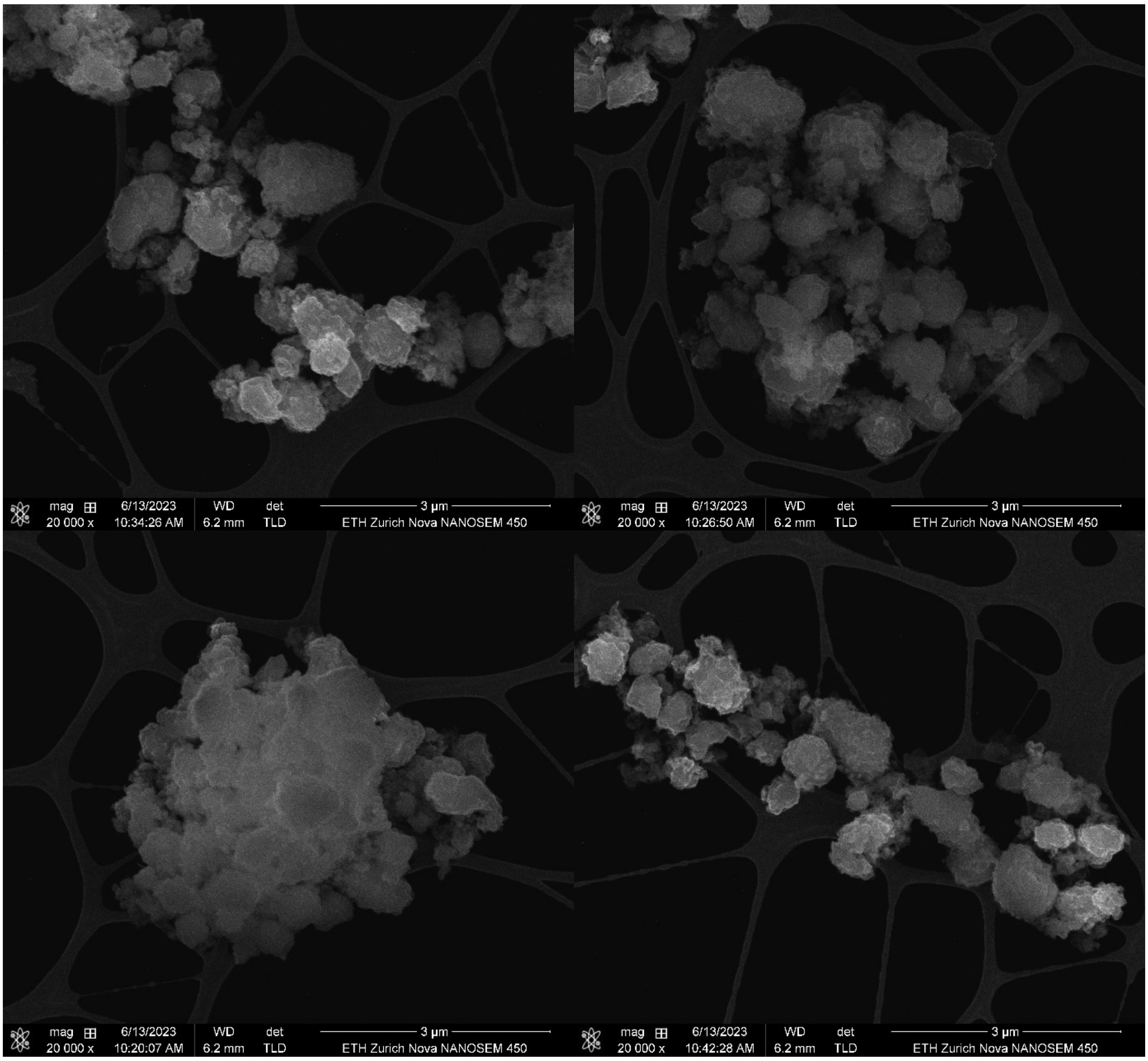

Figure S19. SEM images of BF306 after 20 cycles on TGA at 500 °C

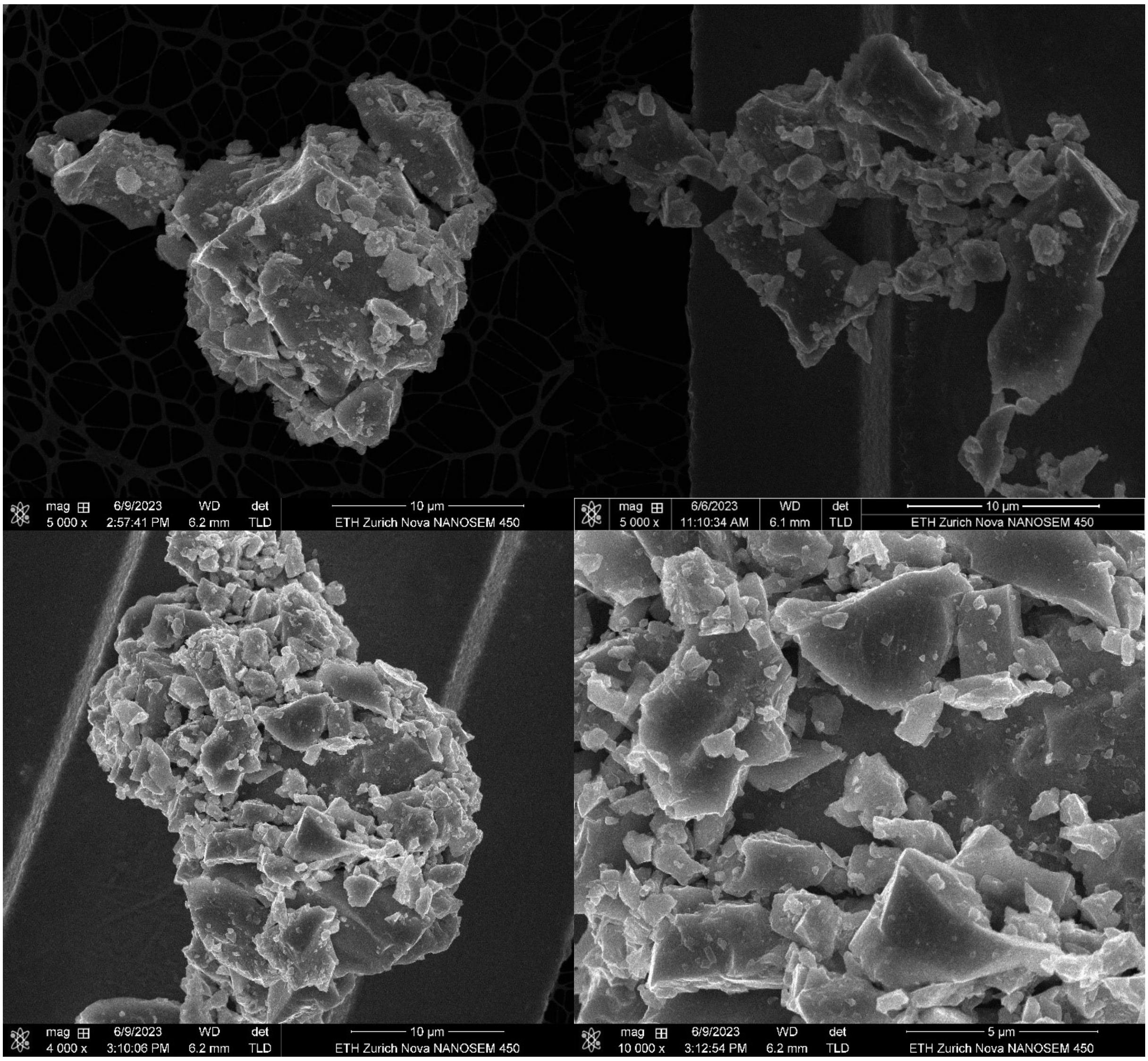

Figure S20. SEM images of iron ore.

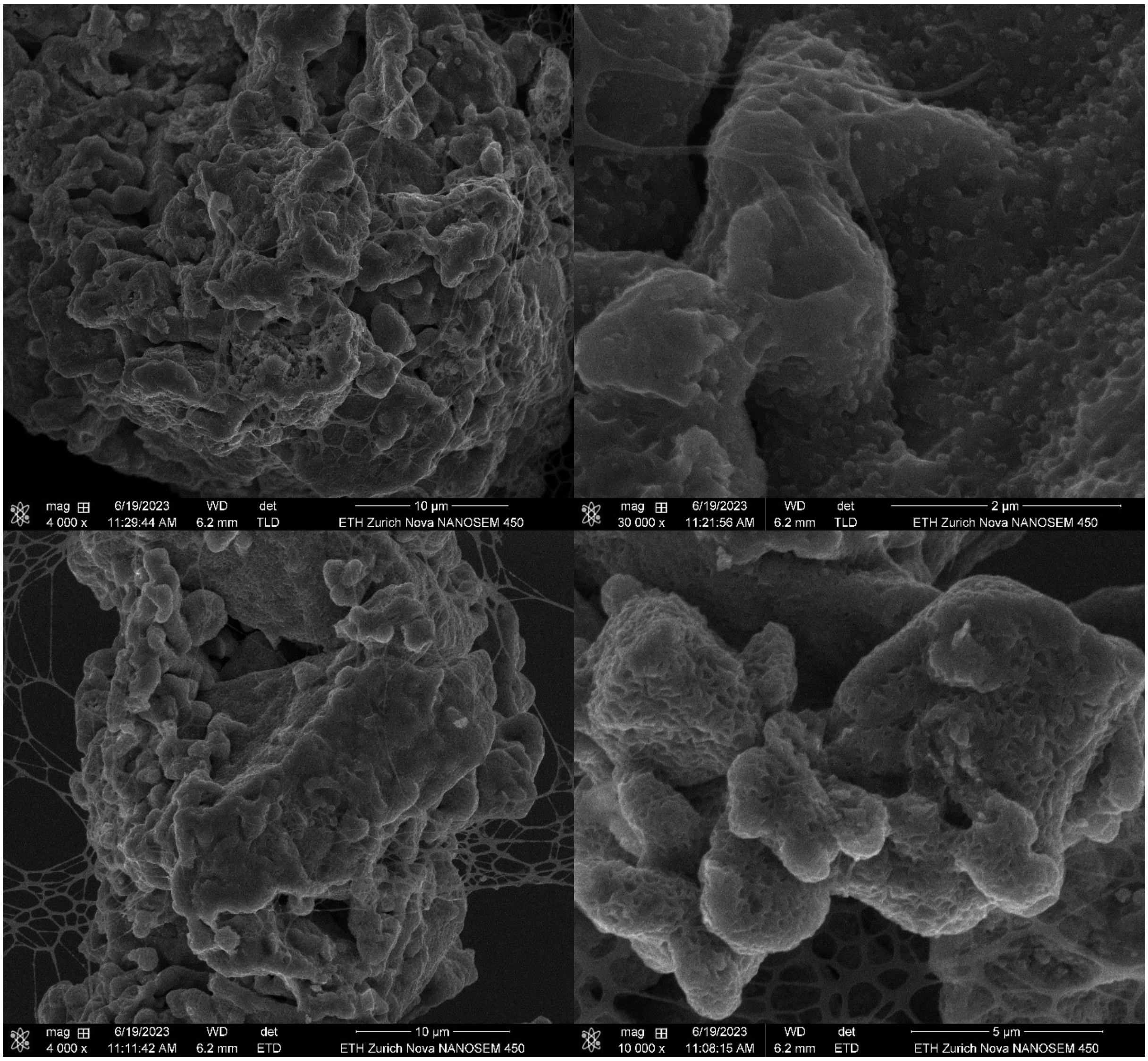

Figure S21. SEM images of iron ore after 20 cycles on TGA at 400 °C

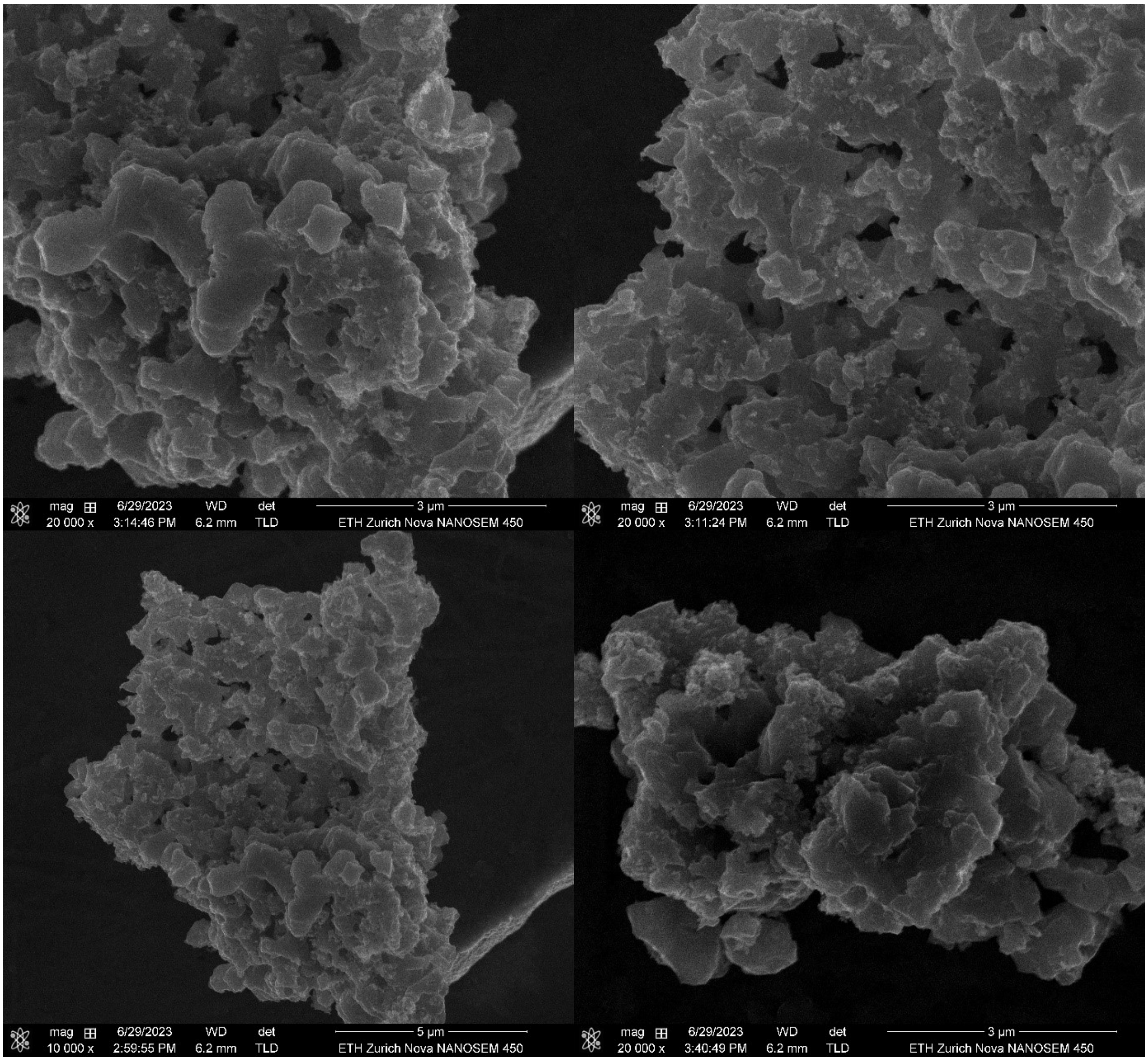

Figure S22. SEM images of iron ore after 20 cycles on TGA at 500 °C

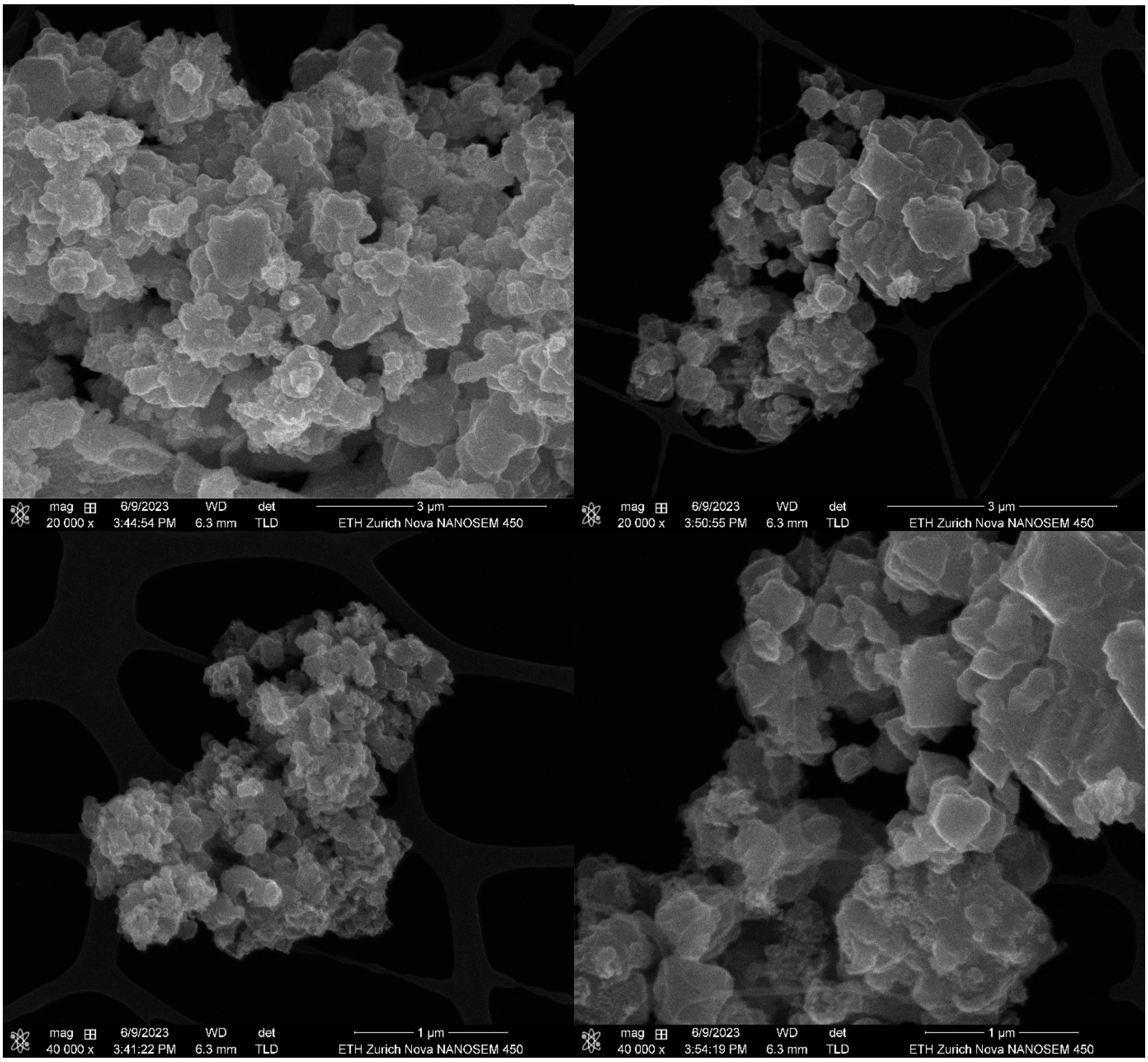

Figure S23. SEM images of iron sample taken from reactor and oxidized in air overnight.

Table S6. The explosion hazards of common dusts[7]

Dust	Mass median diameter μm	Minimum flammable concentration g m^{-3}	K_{st} bar m s^{-1}	Dust hazard class
Sugar	30	200	138	1
Coal, bituminous	24	60	129	1
Wood flour	29	-	205	2
Aluminum	29	30	415	3
Iron, carbonyl	<10	125	111	1
Zinc	<10	125	176	1

Table S7. Comparison of seasonal energy storage pathways

System	Volumetric Storage Density [MWh m^{-3}]	Storage Efficiency [%]	Capital Costs [\$ kWh^{-1}]
Hydrogen (700 bar, Tank)	1.376	82	15 – 25
Hydrogen (200 bar, underground)	0.393	90	2.5
Hydrogen (liquid)	2.408	70	23
Methane (LNG)	5.920	78	0.39
Methane (200 bar, underground)	1.900	78	0.28
Ammonia	4.108	78	1.1 – 6.7
LOHC (Toluene)	1.617	72	1.6 – 2.6
Hydrogen storage alloys	2.872	75	7.3
Steam Iron Process (Ore)	2.089	78	0.57 – 1.95

Supplementary Note 5. Methods for comparison of seasonal energy storage pathways

Different technologies were compared in terms volumetric storage density, efficiency and capital costs, with the following sources:

Storage density: The storage density is based on the values from Steinfeld.[8] The storage density of methane was computed assuming ideal gas law (underground storage), a density of 426 kg m^{-3} (LNG) and a lower heating value of 13.9 kWh kg^{-1}. The storage density of the steam iron process is computed based on the reachable SOC, the bulk density obtained for the ore and the lower heating value of hydrogen is 33.4 kWh kg^{-1}.

Storage efficiency: The storage efficiency is taken from literature (hydrogen 700 bar, tank and hydrogen 200 bar underground),[9] (hydrogen liquid),[10] (ammonia, LOHC (toluene)).[8] The storage efficiency of methane corresponds to the thermodynamic limit taken from Teske.[11] The storage efficiency of the steam iron process and hydrogen storage alloys is taken from Steinfeld.[8] The storage efficiency of the pilot was calculated according to experimentally measured data, by dividing the LHV of the H_2 released during 1st discharging (236.8 kWh) with the total input (heating during discharging: 328.9 kWh; heating during charging: 1407.7 kWh; enthalpy to heat up the water from room temperature to 200 °C in the steam generator: 95.3 kWh; H_2 LHV: 236.8 kWh). The efficiency of the electrolyzer and the fuel cell was not considered, as they are the same for all hydrogen storage techniques.

Cost: The costs are either taken directly from literature data or based on our own estimations. The data for hydrogen storage at 700 bar in a tank and hydrogen at 200 bar underground is taken from Züttel.[12] The data for LOHC is taken from here.[10] The cost of liquefied hydrogen is estimated assuming capital costs for liquid storage tanks of 147 \$ per kg H_2[13] and cost for liquefaction of 118000 \$ per kg H_2 per h[13] with cost adjustment of 2.3 since the data is from 1995. The costs for methane storage are computed assuming cost of 1000 \$ per kW_{CH4} for a methanation unit[11] and 956 \$ m^{-3} for the LNG storage ([14], geometric average of biggest and smallest value) and 0.05 \$ kWh^{-1} for underground storage.[15] The costs for ammonia are computed assuming investment costs of 900 - 5677 \$ kg^{-1} d^{-1} for a Haber Bosch plant and storage costs of 0.1 - 0.2 \$ kWh^{-1}.[16] The cost for hydrogen storage alloys is computed by adding the costs of magnesium[8] and the costs for the storage tank. The costs for the hydrogen storage tank were taken from literature[17] and scaling the system up to 100 MWh assuming the costs scale with a power of $\frac{2}{3}$. The costs of the steam iron process are computed for the size of a 100 household unit and a 1 TWh consumer requiring estimated equipment summarized in Table S8. The equipment costs were computed using correlations taken from.[18] The system is assumed to be at 425°C with 5% conversion per pass. All the equipment costs were multiplied with an installation factor of 5. The cost of iron oxide was estimated as 100 $ t^{-1} and the cost of the insulation was estimated as 50 $ m^{-3} (corresponding to rock wool). For all cost estimations, a constant operation for 6 months during summer is assumed for the charging phase and a constant operation for 4 months during discharging.

Toxicity: The toxicity potential index (TPI) is computed using the model developed by Fraunhofer Institute.[19]

Table S8. Estimated size of the required components and the total system cost for 100 household unit, a storage unit of 1, 10 and 100 GWh and a 1 TWh consumer

Scenario [$MWh_{Storage}$]	**200**	**1000**	**10000**	**100000**	**400000**
Quantity hydrogen stored [kmol](1)	3000	15000	150000	1500000	6000000
Amount of Iron Oxide required [t](2)	216	1080	10800	108000	432000
Cost Iron Oxide [$](3)	21600	108000	1080000	10800000	43200000
Storage vessel size [m^3](4)	108	495	4950	49500	198000
Cost Vessel [$](5),(6)	314000	840000	4320000(7)	43200000	173000000
Characteristic Lenght [m](8)	3.25	5.4	11.6	25	40
Area [m](9)	133	367	1700	7900	19900
Thickness Insulation [m]	0.25	0.5	1	1.5	2
Insulation [m^3](10)	33	183	1700	12000	39800
Cost Insulation [$](11)	1660	9200	85000	590000	1990000
Thermal loss reactor [W](12)	8500	12000	27000	84000	159000
Thermal Loss per year [MWh](13)	75	103	240	740	1395
Storage Efficiency [-](14)	0.60	0.72	0.77	0.78	0.78
Total Gasflow from the hydrogen source [mol s^{-1}](15)	0.19	0.96	9.6	96	385
Assumed Conversion per Pass [-](16)	0.05	0.05	0.05	0.05	0.05
Total Gasflow in System [mol s^{-1}](17)	3.9	19	193	1930	7700
Compressor size [kW](18), (6)	1.59	8.0	80	800	3190
Cost Compressor size [$](19)	32000(20)	890000	1070000	2160000	4570000
Size Heat Exchanger [m^2](21)	8.2	41	410	4100	16400
Cost Heat Exchanger [$](22), (6)	20500	28000	212000	1850000	6900000
Total Cost [$](23)	390000	1870000	6780000	58600000	230000000
Cost per kWh [$ kWh^{-1}](24)	1.95	1.87	0.68	0.59	0.57

(1) Calculated assuming a heating value of 33.4 kWh kg^{-1} and a molar mass of 2 mol g^{-1}.

(2) Assuming a gravimetric storage density of 925 kWh $t^{-1}{}_{Fe3O4}$, which is calculated assuming a molar mass of 231 g mol^{-1}, that 4 mol of H_2 are converted per Fe_3O_4 and that the Fe_3O_4 can be charged by up to 80%.

(3) Calculated assuming a cost of 100 US$ t^{-1}.

(4) Calculated assuming a volumetric density of 2.089 MWh m^{-3}.

(5) Calculated using the cost function of cone roof tanks according to G. Towler and R. Sinnott.[16]

(6) The costs are multiplied with an installation factor of 5 and a material cost factor of 1.3 for stainless steel. Installation factors according to G. Towler and R. Sinnott,[16] and are corrected accordingly with the material cost factors.

(7) The cost functions are interpolation within a certain size range. The range of these tanks however is outside the cost estimate, the cost of these tanks is therefore computed as a number of tanks of 4000 m^3 volume corresponding to the total required volume. The costs per volume decrease with increasing size, the here shown values are therefore an overestimation.

(8) In this example the radius/height is chosen as the characteristic length. The Characteristic length corresponds $L_c = \left(\frac{V_{tank}}{\pi}\right)^{\frac{1}{3}}$ assuming a cylindrical vessel with minimal area.

(9) The minimal area of a cylinder corresponds to $A_{Tank} = 4\,\pi\,L_c^2$.

(10) The volume of the required insulation corresponds to $V_{iso} = A_{Tank} \cdot d_{iso}$, where d_{iso} corresponds to the thickness of the cylinder.

(11) The cost of the insulation corresponds to $C_{iso} = 50\ \$\ m^{-3} \cdot V_{iso}$. The cost factor of $50\ \$\ m^{-3}$ corresponds to the cost of rock wool per m^3.

(12) The thermal loss of the reactor is computed using the formula below

$$\dot{Q}_{loss,Reactor} = \frac{A_{tank}\lambda_{iso}}{d_{iso}}\left(T_{tank} - T_{outside}\right).$$

In this example, the reactor temperature is assumed as 400°C and the outside temperature as 25 °C. Both temperatures are assumed to remain constant through the year. The thermal conductivity of the insulation averaged from 25°C to 400°C is estimated as 0.04 $W\,m^{-1}\,K^{-1}$, which corresponds the value for rockwool.

(13) The thermal loss of the reactor multiplied by the time of one year.

(14) The storage efficiency $\eta_{Storage}$, which is computed to the equation shown below, corresponds to the ratio of the total amount of releasable energy in form of hydrogen $E_{hydrogen,out}$ and the sum over all energy inputs. The energy inputs correspond to the energy inputs required to compensate the thermal losses over one year $E_{loss,reactor}$, the energy consumed by the compressor during one year $E_{compressor}$, the energy required to compensate for losses in the pipes and the heat exchanger $E_{loss,pipes}$, the energy

required to evaporate water for the discharge process E_{evap}, the energy needed to compensate the endothermal reaction during the charging cycle $E_{reaction}$ and the energy supplied to the system in the form of hydrogen $E_{hydrogen,in}$.

(15) $$\eta_{Storage} = \frac{E_{hydrogen,out}}{E_{loss,reactor} + E_{compressor} + E_{loss,pipes} + E_{evap} + E_{reaction} + E_{hydrogen,in}}$$

The ratio $\frac{E_{hydrogen,out}}{(E_{loss,pipes} + E_{evap} + E_{reaction} + E_{hydrogen,in})}$ corresponds to the maximum achievable efficiency η_{max}, (78%[8]) and $E_{hydrogen,out}$ is equal to $E_{hydrogen,in}$ as nearly no hydrogen is lost during the storage process.

(16) The total gas flow from the hydrogen source corresponds to the amount of hydrogen supplied during the 180 days required for a charging.

(17) The conversion per pass is estimated to correspond to half the thermodynamically possible conversion.

(18) The total gas flow in the system corresponds to the total gas flow supplied by the hydrogen source divided by the conversion per pass.

(19) Calculated assuming adiabatic compression of a diatomic ideal gas using the formula shown below:

$$\dot{W}_{adiabatic,real} = \frac{5}{2\eta_{real}} \dot{n} R T_{in} \left(\left(\frac{p_{out}}{p_{in}} \right)^{\frac{\frac{7}{5} - 1}{\frac{7}{5}}} - 1 \right)$$

The compressors in this example are computed assuming an inlet pressure p_{in} of 1 bar, an outlet pressure p_{out} of 1.2 bar, an inlet temperature T_{in} of 298.15 K, an efficiency η_{real} of 0.8, the gas constant R corresponding to 8.314 J K^{-1} mol^{-1} and a total gas flow $\dot{n}$.

(20) The compressor costs were calculated using the cost function of a reciprocating compressor according to G. Towler and R. Sinnott.[16]

(21) A compressor of this size, would be outside the range of the cost function by G. Towler and R. Sinnott.[16] The costs are estimated of a device recently purchased with similar power consumption.

(22) The heat exchanger area A_{Hex} was estimated using the formula below:

$$A_{Hex} = \eta_{Hex} \frac{\dot{n} c_p \Delta T}{Nu \frac{\lambda_{H2}}{d_{plate}} \Delta T_{lm}}$$

In this example the heat exchanger area is computed using the total gas flow rate $\dot{n}$, the isobaric heat capacity c_p of a diatomic ideal gas corresponding to $\frac{7}{2}R$, the temperature difference between inlet and outlet ΔT, corresponding to 375°C, the fraction of integrated heat η_{Hex}, which accounts for thermal losses which are not integrated, corresponding to 0.9, the log mean temperature difference ΔT_{lm}, corresponding to 10°C, the thermal conductivity of hydrogen λ_{H2}, which was approximated with the thermal conductivity at 200°C (0.268 W $K^{-1}m^{-1}$) and the distance between two plates d_{plate} and the Nusselt number, which for laminar flow between two plates corresponds to 3.66.

(23) Calculated using the cost function of a plate and frame heat exchanger according to G. Towler and R. Sinnott.[16]

(24) Corresponding to the sum of the costs of the iron oxide, the vessel, the compressor, the insulation and the heat exchanger. The total costs correspond to an approximation of the total investment costs needed to build this system.

(25) Corresponding to ratio of total investment costs to energy stored in the system described.

Supplementary Note 6. Case modelling

To demonstrate the practical viability beyond the 210 L scale and to assess the overall costs of such system in real world, an optimization was conducted minimizing the overall levelized cost of energy while reliably supplying the consumer with energy according to his demand. The methodology used is a simplification of the methodology presented by Gabrielli et al.[9]

For the different scenarios the following assumptions were made:

The energy system consists of the following units: A PV installation supplying electricity to the storage units and the consumer, a battery or pumped hydro plant (depending on the scenario) for diurnal energy storage, a unit for seasonal storage containing an electrolyzer, a fuel cell and a steam iron process unit. Lastly a consumer is present consuming electricity according to a predefined demand.

The overall cost function is the sum of the costs of the different components: PV, electroylzer, fuel cell, steam iron process and battery (10).

$$\min C(x) = C_{PV} + C_{El} + C_{FC} + C_S + C_B \#(10)$$

To ensure sufficient supply of electricity to the consumer, constraint (11) is imposed for all times t on the optimization. $P_{PV,t}$ represents the amount of electricity produced by PV at time t. $P_{PV,t}$ is the product of the installed capacity S_{PV} and the generation curve $c_{S,t}$ (12). $c_{S,t}$ corresponds to the estimated averaged PV production.[1] $P_{B,t}$ is the amount of energy coming from the battery and $P_{S,t}$ from the steam iron process at time t. Negative values of $P_{B,t}$ and $P_{S,t}$ indicate energy being transferred into the storage unit. $P_{D,t}$ is the energy demanded by the consumer, which is based on the total electricity consumption in 2017[2] scaled to the total expected consumption used in the different scenarios. Both $P_{S,t}$ and $P_{D,t}$ are resolved to an hourly level, resulting in 2 x 8760 + 1 design variables 8760 x $P_{B,t}$, 8760 x $P_{S,t}$ and S_{PV}. To lower computational cost, 12 design days capturing the average consumption and production of a given hour within a month are used to reduce the number of design variables to 577.

$$P_{PV,t} + P_{B,t} + P_{S,t} - P_{D,t} \geq 0 \#(11)$$

$$P_{PV,t} = S_{PV} c_{S,t} \#(12)$$

The different unit sizes and costs were computed using the following models:

The solar cell costs correspond to the peak production of the cell S_{PV} multiplied with a corresponding cost factor (13).

$$C_{PV} = S_{PV}c_{PV}\#(13)$$

Fuel cell and the electrolyzer are sized according to the maximum and minimum value of $P_{S,t}$, which represent the maximum release (fuel cell) and the maximum absorption (electrolyzer) of electricity. The maximum release corresponds to the highest amount of electricity supplied by the storage unit, which corresponds to the fuel cell size (14). Similarly, the minimum of power transferred to the storage unit determines the size of the electrolyzer (15). The cost of both units is computed by multiplying their respective size with a cost factor.

$$C_{FC} = \mathrm{c}_{FC}\max\left(P_{S,t}\right)\#(14)$$

$$C_{El} = \mathrm{c}_{El}\min\left(P_{S,t}\right)\#(15)$$

The size of storage units depends on the integral properties of total stored energy in the storage system. Sizing the battery and the seasonal storage unit requires knowing the total amount of energy within each storage unit at all times. The energy $E_{S,t}$ in the seasonal storage unit or $E_{B,t}$ in the battery corresponds to the previous amount of stored energy $E_{j,t-1}$ and the change within the last hour $P_{j,t}$, which in case of flows into the storage unit are multiplied with the round-trip efficiency to account for losses (16, 17).

$$E_{S,t} = E_{S,t-1} + P_{S,t}\psi\left(P_{S,t}\right)\#(16)$$

$$E_{B,t} = E_{B,t-1} + P_{B,t}\psi\left(P_{B,t}\right)\#(17)$$

$$\psi\left(P_{k,t}\right) = \begin{cases} 1\ if\ P_{i,t} \geq 0 \\ \eta_i,\ else \end{cases}\#(18)$$

The difference between the maximum and minimum level of energy in the storage unit divided by the efficiency of the discharge step corresponds the size of the storage unit (19,20). The size multiplied with the cost factor corresponds to the storage unit cost.

$$C_S = c_S\frac{\max\left(E_S\right) - \min\left(E_S\right)}{\eta_{FC}}\#(19)$$

$$C_B = c_B\max\frac{\max\left(E_{B,j}\right) - \min\left(E_{B,j}\right)}{\eta_B}\#(20)$$

Furthermore, the battery is used for only day-night storage, it should therefore be at the same level of charge after 24 h leading to 12 additional, nonlinear constraints (21). Similarly, the amount of energy supplied into the seasonal storage unit should correspond to the energy delivered into the reactor adjusted with the storage efficiency (22)

$$\sum_{t_{day}} P_{B,t}(P_{B,t} > 0) + \sum_{t_{day}} \eta_B P_{B,t}(P_{B,t} < 0) = 0\#(21)$$

$$\sum_{t\,=\,1}^{t_{End}} P_{S,t}(P_{S,t} > 0) + \sum_{t=1}^{t_{End}} \eta_S P_{S,t}(P_{S,t} < 0) = 0\#(22)$$

To account for the life time of the equipment the cost factor is computed by (23), where I_j are the total investment costs per kW or kWh depending on the unit. j corresponds to the year in which the investment was made, and *r* is the interest rate, which was fixed to 5% (Operating and maintenance costs are not considered in this analysis).

$$c_j = \sum_{j=0}^{25} \frac{I_j}{1 + r^j}\#(23)$$

The total levelized costs of energy is computed with (24), where *C* are the total annualized costs computed by the cost function (10) and E_j is the energy produced in year *j*

$$LCOE = \frac{C}{\sum_{j=0}^{25} \frac{E_j}{1 + r^j}}\#(24)$$

The following scenarios were modelled:

Scenario 1: A single household which is supplied with PV consuming 4500 kWh of electricity per year

Scenario 2: A community of 100 households which are supplied with PV consuming 4500 kWh of electricity per year each

Scenario 3: A large consumer of 1 TWh electricity which is supplied with PV

For the different scenarios different cost assumptions are made for the year 2020 and 2030, which are summarized in Table S9. The costs of the different units are based on literature and in case of the seasonal storage unit on our estimations. For all estimations 12 design days were used corresponding to each month of the year. The optimization was solved using MATLAB R2021b and the solver fmincon and the interior point algorithm.

Table S9. Costs and efficiencies for different components in the simulations for the different scenarios and years, with their corresponding equipment life time

Scenario	Scenario 1, year 2020	Scenario 1, year 2030	Scenario 2, year 2020	Scenario 2, year 2030	Scenario 3, year 2020	Scenario 3, year 2030	Equipment Life time 2020	Equipment Lifetime 2030
PV [$/kW_p]	1500a)	900b)	1500a)	700b)	1500a)	530b)	25c)	25c)
Battery [$/kWh]	1000a)	230a)	563d)	100c)	-	-	8c)	12e)
Efficiency Battery [%]	85a)	95e)	90c)	95e)	-	-	-	-
Pumped Hydro Plant [$/kWh]	-	-	-	-	19f)	19f)	80c)	80c)
Efficiency Pumped Hydro Plant [%]	-	-	-	-	70g)	70g)	-	-
Electrolyzer [$/kW]	3333h)	1000c)	1800i)	1000c)	1800i)	1000c)	15j)	15j)
Efficiency Electrolyzer [%]	68k)	68k)	68k)	68k)	68k)	88c)	-	-
Fuel Cell [$/kW]	20000l)	1000a)	10000l)	1000a)	1000m,l)	1000a)	15l)	15l)
Efficiency Fuel Cell [%]	50l)	60l)	50l)	70l)	40m,n)	60l)	-	-
Steam Iron Process [$/kWh]	16.6h)	16.6h)	1.95o)	1.95o)	0.57o)	0.57o)	25p)	25p)
Efficiency Steam Iron Process [%]	50p)	50p)	60p)	60p)	78q)	78q)	-	-

a) [20], b) [21], c) [12], d) Cost of a Tesla Power Wall e) [4], f) [5], g) [22], h) Estimates based on real prices payed for scale-up to this size from a currently running project, i) Geometric average FC costs at small scale 2020 and 2030 price, j) [23], k) [24], l) [25], m) Hydrogen is combusted using turbine, n)Average efficiency of in simple cycle turbines from Mitsubishi Heavy Industries, Ltd.,[26] o) Estimates taken from Supplementary Note 5, p) Own estimate, q) [8].

Table S10. Comparison of batteries and iron/iron oxide used for seasonal energy storage

Technology	Raw material cost [$ t^{-1}]	Energy density [kWh t^{-1}]	Cost of metal per energy stored [$ kWh^{-1}]
Vanadium flow battery	26250[a)]	50[b)]	99[c)]
Li-ion battery	23500[d)]	350[e)]	67[f)]
Fe/FeO_x	120[g)]	954[h)]	0.13

[a)] Current price of Ferro Vanadium containing 80 wt% V, was 45000 $/t in Feb 2023. [b)] Theoretical max value.[27] This is limited by the solubility of V^{2+}, V^{3+}, VO^{2+} and VO2^{+}, typically no more than 3 mol/L.[28] [c)] Assuming $E_0 = 1.26$ V, giving max possible $\Delta G = nFE_0 = 1*96485*1.26 = 121571$ J. One mole of this reaction requires 2 mol V, which is 101.8 g. This means a minimum of 3.01 kg V per kWh of stored electricity is required. [d)] Current cost of battery grade $LiOH{\cdot}H_2O$ (16 wt% Li), was 31500 $/t in Apr 2023. [e)] Current value for electric car batteries (cell alone, the energy density of the whole pack is lower at 250 kWh/t).[29] [f)] Assuming a cell contains 11 wt% Li. The costs for the anode and electrolyte are not considered. [g)] Current price of iron ore containing 62 wt% Fe. [h)] Based on the stoichiometry of Fe_3O_4 and H_2, and the lower heating value of H_2 (119.96 MJ/kg).

References

1. C.-T. Chu and A. D. Hawkes, *Energy*, 2020, **193**, 116630.
2. Swissgrid AG, Energieübersicht Schweiz 2017, https://www.swissgrid.ch/de/home/operation/grid-data/generation.html, (accessed June 2023).
3. A. Toktarova, L. Gruber, M. Hlusiak, D. Bogdanov and C. Breyer, *Int. J. Electr. Power Energy Syst.*, 2019, **111**, 160-181.
4. IRENA, *Electricity Storage and Renewables: Costs and Markets to 2030*, International Renewable Energy Agency, Abu Dhabi, 2017.
5. Directorate-General For Energy, Database of the European Energy Storage Technologies and Facilities [Data Set], https://doi.org/10.2906/101110101114/1, (accessed June 2023).
6. U. B. Lustenberger, PhD Thesis, ETH Zürich, 2022.
7. NFPA, Guide for Venting of Deflagrations, Quincy, MA, USA, 2002.
8. L. Brinkman, B. Bulfin and A. Steinfeld, *Energy Fuels*, 2021, **35**, 18756-18767.
9. P. Gabrielli, M. Gazzani, E. Martelli and M. Mazzotti, *Appl. Energy*, 2018, **219**, 408-424.
10. Bundesamt für Energie, Etude de reconversion du site de la raffinerie de Collombey, Opporunité d'utilisation de l'hydrogène sous forme de "liquid organic hydrogen carriers" (LOHC), https://www.aramis.admin.ch/Default?DocumentID=66988&Load=true, (accessed June 2023).
11. S. L. Teske, M. Rüdisüli, C. Bach and T. Schildhauer, *Potentialanalyse Power-to-Gas in der Schweiz*, Empa (Dübendorf) & Paul Scherrer Institut (Villigen PSI), 2019.
12. A. Züttel, N. Gallandat, P. J. Dyson, L. Schlapbach, P. W. Gilgen and S. I. Orimo, *Front. Energy Res.*, 2022, **9**, 1-17.
13. W. A. Amos, Cost of Storing and Transporting Hydrogen, https://www.nrel.gov/docs/fy99osti/25106.pdf, (accessed June 2023).
14. LNG ISO tank: Get overview of features, types & sizes [+2022 best price], https://www.container-xchange.com/blog/lng-iso-tank/, (accessed June 2023).
15. P. Jelušič, S. Kravanja and B. Žlender, *J. Nat. Gas Sci. Eng.*, 2019, **61**, 142-157.
16. G. Towler and R. Sinnott, *Chemical Engineering Design: Principles, Practice and Economics of Plant and Process Design*, Butterworth-Heinemann, Burlington, MA 2022.
17. G. Amica, P. Arneodo Larochette and F. C. Gennari, *Int. J. Hydrogen Energy*, 2020, **45**, 18789-18801.
18. G. Towler and R. Sinnott, *Chemical Engineering Design: Principles, Practice and Economics of Plant and Process Design*, Butterworth-Heinemann, 2008.
19. Fraunhofer Institute for Reliability and Microintegration, Toxic Potential Indicator (TPI), https://www.izm.fraunhofer.de/en/abteilungen/environmental_reliabilityengineering/key_research_areas/environmental-assessment-for-electronic-systems/toxic-potential-indicator--tpi-.html, (accessed June 2023).
20. M. Y. Haller, D. Carbonell, M. Dudita, D. Zenhäusern and A. Häberle, *Energy Convers. Manage.: X*, 2020, **5**, 100017.
21. E. Vartiainen, G. Masson and C. Breyer, PV LCOE in Europe 2014-2030 - Final Report., https://etip-pv.eu/publications/etip-pv-publications/download/pv-costs-in-europe-2014-2030, (accessed June 2023).
22. P. C. Nikolaos, F. Marios and K. Dimitris, *Energies*, 2023, **16**, 4516.

23. IRENA, *Green Hydrogen Cost Reduction: Scaling up Electrolysers to Meet the 1.5ºC Climate Goal*, International Renewable Energy Agency, Abu Dhabi, 2020.
24. International Energy Agency, The Future of Hydrogen: Seizing Today's Opportunities, https://www.iea.org/reports/the-future-of-hydrogen, (accessed June 2023).
25. International Energy Agency, Technology Roadmap, Hydrogen and Fuel Cells, https://www.iea.org/reports/technology-roadmap-hydrogen-and-fuel-cells, (accessed June 2023).
26. Mitsubishi Heavy Industries, *Hydrogen Power Generation Handbook*, 2019.
27. Z. Huang, A. Mu, L. Wu, B. Yang, Y. Qian and J. Wang, *ACS Sustainable Chem. Eng.*, 2022, **10**, 7786-7810.
28. E. Sánchez-Díez, E. Ventosa, M. Guarnieri, A. Trovò, C. Flox, R. Marcilla, F. Soavi, P. Mazur, E. Aranzabe and R. Ferret, *J. Power Sources*, 2021, **481**, 228804.
29. J. Duan, X. Tang, H. Dai, Y. Yang, W. Wu, X. Wei and Y. Huang, *Electrochemical Energy Reviews*, 2020, **3**, 1-42.